

https://dspace.org/

Design of a reluctance synchronous machine for traction motor applications using the finite element method

Wright, Jarrad G

2011-11-02
http://hdl.handle.net/10539/10685

Downloaded from a DSpace repository. https://dspace.org/

DESIGN OF A RELUCTANCE SYNCHRONOUS MACHINE FOR TRACTION MOTOR APPLICATIONS USING THE FINITE ELEMENT METHOD

Jarrad G. Wright

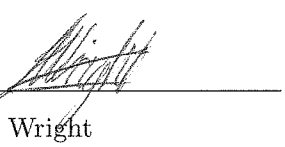
A dissertation submitted to the Faculty of Engineering and the Built Environment, University of the Witwatersrand, Johannesburg, in fulfilment of the requirements for the degree of Master of Science in Engineering.

University of the Witwatersrand, Johannesburg, 2010

Declaration

I declare that this dissertation is my own, unaided work, other than where specifically acknowledged. It is being submitted for the degree of Master of Science in Engineering in the University of the Witwatersrand, Johannesburg. It has not been submitted before for any degree or examination in any other university.

Signed this 17th day of November 2010



Jarrad G. Wright

Abstract

Traction motors, specifically in underground shuttle vehicles, often operate in harsh conditions including steep grades, heavy payloads and high ambient temperatures. These motors require maximum torque density as well as cool and robust operation in order to optimise the overall process and to avoid the current requirement for a duty cycle. The contribution of this research is the design of a new traction motor, a Reluctance Synchronous Machine (RSM), via the 2-D Finite Element Method (FEM) as the primary engineering design tool to replace the commonly used Induction Machine (IM). The electromagnetic and mechanical design of the RSM are performed in commercially avaliable FEM software packages FLUX and ANSYS respectively. The electromagnetic design uses the PyFLUX command language and Python scripting to vary five rotor geometric parameters in a linear progression to find where maximum average torque and minimum torque ripple occurs for each parameter. The mechanical strength of the RSM rotor is defined by two geometric parameters whose final values are chosen via a case study based design in ANSYS. The newly designed RSM runs much cooler than the original IM and develops only 8.4% less torque than the IM. As a result, it should not require a duty cycle and will be capable of a higher rating and thus more torque can be delivered to the end process (up to 42% more) while the motor remains in the same motor frame size. Furthermore, there is a large area of research pertaining to the overall electromagnetic design method used. This includes the use of optimisation algorithms, integrated rotor-stator design, mechanical support placement and grading, various torque ripple reduction techniques and the inclusion of permanent magnets or composite powder metals for the RSM rotor.

To my parents, family and friends

To my one true love, Téhne

Acknowledgements

I would like to sincerely thank:

My supervisor Prof. W.A. Cronje for his guidance and experienced insight.

The many people at the School of Electrical and Information Engineering at the University of the Witwatersrand - Mr. A. Meyer, Prof. I. Hofsajer, Mr. H. Fellows and fellow postgraduate students.

Mr M. Pardini and Mr S. Pardini at Transvaal Electric (Pty) Ltd for the initial project conception.

The University of the Witwatersrand and The National Research Foundation (NRF) for giving me the opportunity to complete my postgraduate studies.

Contents

Declaration ii

Abstract iii

Acknowledgements v

Contents vi

List of Figures ix

List of Tables xi

List of Symbols xii

1 Introduction and Background 2

1.1 Brief background and general problem statement 2

1.2 General hypothesis and solution formulation 4

1.3 Dissertation layout 5

2 Reluctance Synchronous Machine (RSM) Fundamentals 6

2.1 VSDs in brushless AC drives 6

2.2 RSM as an industrial solution 7

2.3 RSM brief history and background 8

2.4 Analytical model 9

2.5 Control fundamentals 15

2.5.1 Ideal RSM control 15

2.5.2 Parameter effects on RSM control 16

2.5.3 Effects of iron loss and saturation 17

2.6 Summary 20

3 RSM Finite Element Modelling and Design Procedure 21

3.1 FEM background 21
3.1.1 Basics of FEM 21
3.1.2 Electromagnetic application of FEM 22
3.1.3 Magnetostatic field problem 24
3.2 RSM electromagnetic design 25
3.2.1 Background 25
3.2.2 Hardware and software requirements 26
3.2.3 Electromagnetic design procedure 27
3.2.4 Electromagnetic design implementation in FLUX® 29
3.2.5 Magnetisation curve for electromagnetic FEM simulations . . 32
3.2.6 Mesh for electromagnetic FEM simulations 32
3.2.7 Electromagnetic FEM design results 34
3.2.8 Final electromagnetic design 41
3.3 Mechanical FEM case studies 43
3.3.1 Types of mechanical analyses 44
3.3.2 Types of loads 44
3.3.3 Mechanical FEM design results 45
3.4 Inductances of the final RSM design 49
3.5 Electromagnetic performance of RSM case studies 52
3.5.1 Comparison of Case I with Case II 52
3.5.2 Comparison of Case II with Case III 53
3.6 Summary 54

4 Comparison of RSM and IM Simulation Results 58
4.1 RSM and IM cross sections 58
4.2 RSM and IM comparison 58
4.3 RSM and IM comparison with RSM operating at MTC 59
4.4 RSM and IM thermal comparison 60
4.5 RSM and IM comparison considering saturation 61
4.6 Summary 62

5 RSM Research Suggestions and Future Work 64
5.1 RSM design improvements 64
5.1.1 Direct use of optimisation algorithms in FEM design 64
5.1.2 Integrated rotor-stator design 65
5.1.3 Air-gap length 65

5.1.4 Choice of rotor barrier shape 66
5.1.5 Rotor mechanical supports 66
5.1.6 Inclusion of rotor cage in RSM rotor 67
5.1.7 Torque ripple reduction 68
5.1.8 Permanent magnet assisted RSM 71
5.1.9 Composite powder metal RSM rotor 71
5.1.10 3-D FEM analysis 72
5.2 Summary 73

6 Conclusion **74**

References **76**

A Example Python File used in electromagnetic design **81**

B Geometric details of the RSM design **87**
B.1 Stator geometric details 87
B.2 Rotor geometric details 88
B.3 Final stator and rotor 88

C Technical details of original IM **91**

D Published Work **93**

List of Figures

2.1 Two fundamental rotor topologies for RSMs with 4-pole rotors . . . 10
2.2 Equiflux plot of RSM illustrating reluctance torque 11
2.3 D and Q-axis equivalent circuits of RSM 12
2.4 Phasor diagram of RSM including iron losses 13
3.1 Example mesh with four nodes and one complete element 22
3.2 Geometric parameters of a TL RSM rotor 27
3.3 Example torque waveforms as a function of rotor angle 29
3.4 Linear progression approach for design procedure 30
3.5 Modular structure of Python files used for electromagnetic design . . 33
3.6 Magnetisation curve used for electromagnetic FEM 34
3.7 Example of the mesh used in electromagnetic simulations 35
3.8 Zoomed views of electromagnetic mesh 36
3.9 Mean torque and torque ripple versus beta for a range of rotor barriers 38
3.10 Torque versus position of first rotor barrier W_p 39
3.11 Torque versus pole pitch to pole span ratio α 40
3.12 Torque versus air-gap length 41
3.13 Torque versus lengths of rotor supports 42
3.14 Cross section of RSM rotor after electromagnetic design 43
3.15 von Mises stress plots for Case I 46
3.16 Displacement contour plot for Case I 47
3.17 von Mises stress plots for Case II 48
3.18 Displacement contour plot for Case II 49
3.19 von Mises stress plots for Case III 50
3.20 Displacement contour plot for Case III 51
3.21 RSM cross section after electromagnetic and mechanical design . . . 52
3.22 Equiflux plots with D and Q axis excitation 53
3.23 Flux density waveforms with D and Q-axis excitation 54
3.24 D and Q axis magnetising inductances for a range of currents 55

3.25 Torque index of final RSM rotor 55
3.26 Comparison of torque with straight and rounded barrier edges 56
3.27 Equiflux plots for Cases I and II 57
3.28 Comparison of torque with different mechanical support widths . . . 57
4.1 Cross section of original IM 59
4.2 Cross section of final RSM 60
4.3 Typical RSM torque versus current angle curve 61
4.4 Torque of final designed RSM with 140% rated current 62
5.1 Pure steel rotor to investigate shape of D-axis flux lines 67
5.2 RSM rotor with graded mechanical supports 68
5.3 TL RSM rotor with radial ribs in new positions (off the Q-axis) . . . 69
5.4 TL RSM rotor with rotor cage included in rotor barriers 70
5.5 Zoomed view of typical RSM torque versus current angle 70
5.6 TL RSM rotor with embedded permanent magnets 72
B.1 Geometric dimensions of one stator slot 87
B.2 Geometric dimensions of stator lamination 88
B.3 Geometric details of final RSM rotor lamination 89
B.4 Final RSM rotor inside original stator 90
C.1 Cross section of modelled original IM 92

List of Tables

3.1 Parameters to be changed during electromagnetic design procedure. 26

3.2 Final values of geometric parameters after electromagnetic design . . 42

3.3 Stresses and safety factors for three mechanical FEM investigations . 51

C.1 Original Induction Machine (IM) technical specifications 91

List of Symbols

Variables

$[X]$	Multidimensional input vector used in design optimisation
$[Y]$	Output function value used in design optimisation
α	Pole pitch to pole span ratio
β	Rotor insulation ratio
ϵ	Electric permittivity
γ	Rotor barrier pitch
κ	Stator slot pitch
λ_{dm}	D-axis magnetising flux linkage
λ_{dqs}	Stator flux linkage space vector
λ_{ds}	D-axis stator flux linkage
λ_{qm}	Q-axis magnetising flux linkage
λ_{qs}	Q-axis stator flux linkage
μ	Magnetic permeability
ν	Poisson's ratio
ω_m	Mechanical angular velocity
ω	Electrical angular velocity
ψ_n	Asymmetrical angle shift of n_{th} pole barrier
ρ	Density of electric charge
σ	Electric conductivity
$\mathbf{A}$	Magnetic vector potential
$\mathbf{B}$	Magnetic flux density
$\mathbf{D}$	Electric field displacement
$\mathbf{E}$	Maxwell's electric field (sum of the Coulomb and induced field)
$\mathbf{H}$	Magnetic field strength

$\mathbf{J}$	Current density
θ_i	Current vector angle from the D-axis (electrical)
ξ_m	Magnetising saliency ratio
ξ	True saliency ratio
ζ	Torque Index
a	a_{th} element in torque waveform
B_{1d}	Fundamental component of D-axis air-gap flux density waveform
B_{1q}	Fundamental component of Q-axis air-gap flux density waveform
b_{bw}	Individual rotor barrier width
B_{eq}	Combined friction coefficient of machine and load
b_{lw}	Individual flux guide width
D	Stator bore diameter
E_y	Young's modulus
i_{ds}^*	D-axis current estimation calculated from estimations of the Reluctance Synchronous Machine (RSM) parameters
i_{dm}	D-axis magnetising current
i_{dqm}^G	Magnetising current space vector in generator mode
i_{dqm}	Magnetising current space vector
i_{dqs}^G	Terminal current space vector when in generator mode
i_{dqs}	Stator current space vector
i_{ds}	Stator terminal current in the D-axis
I_p	IM and RSM individual stator winding peak current $= \frac{I_{rated}}{2}\sqrt{2}$
i_{qm}^G	Stator Q-axis magnetising current when in generator mode
i_{qm}	Q-axis magnetising current
i_{qs}^G	Stator Q-axis terminal current when in generator mode
i_{qs}	Stator terminal current in the Q-axis
I_{rated}	Rated current of original induction machine
J_{eq}	Combined moment of inertia of machine and load
K_w	Fundamental winding factor
L_{dm}	D-axis magnetising inductance
l_{Fe}	Effective stack length
L_{qm}	Q-axis magnetising inductance
l_{rr}	Length of the radial ribs
$L_{s\sigma}$	Stator per phase leakage inductance

l_{tw} Length of the tangential webs

N_1 Number of turns per phase

N_c Number of parallel circuits per phase

n_r Number of separation points per pole pair on the RSM rotor

n_s Number of stator slots per pole pair

N Total number of elements in torque waveform

n Relevant pole number in asymmetrical rotor design

P Number of pole pairs in the machine

R_m Equivalent iron loss resistance

R_s Stator per phase resistance

T_{ea} Value of torque at the a_{th} position in torque waveform

T_{el} Electromagnetic torque

T_{max} Maximum torque in torque waveform

T_{mean} Mean torque of torque waveform

T_{mech} Mechanical load torque

T_{min} Minimum torque in torque waveform

T_{ripple} Calculated torque ripple

V_{ds} Stator voltage in the D-axis

V_{qs} Stator voltage in the Q-axis

2-D 2-dimensional

3-D 3-dimensional

3-Φ three-phase

ALA Axially Laminated Anisotropy

CAC Constant Angle Control

CCIAC Constant Current in Inductive Axis Control

DOL Direct On-line

EIE School of Electrical and Information Engineering

EMF Electromotive Force

EMI Electromagnetic Interference

FEA	Finite Element Analysis
FEM	Finite Element Method
GMRES	Generalised Minimum Residual Method
HVF	Harmonic Voltage Factor
ILUT	Incomplete LU factorisation with Threshold
IM	Induction Machine
LUT	Look-Up Table
MEC	Maximum Efficiency Control
MMF	Magneto-motive Force
MPFC	Maximum Power Factor Control
MRCTC	Maximum Rate of Change of Torque Control
MRG	Machines Research Group
MTC	Maximum Torque Control
PI	Proportional Integral
PM	Permanent Magnet
PMa-RSM	Permanent Magnet assisted Reluctance Synchronous Machine
PMSM	Permanent Magnet Synchronous Machine
RLSE	Recursive Least of Squares Estimator
RSM	Reluctance Synchronous Machine
SRM	Switched Reluctance Machine
SM	Synchronous Machine
SVM	Space Vector Modulation
TL	Transversely Laminated
TVE	Transvaal Electric (Pty) Ltd
VSD	Variable Speed Drive
WITS	University of the Witwatersrand

Chapter 1

Introduction and Background

An introduction to underground shuttle vehicles is given with specific interest in the replacement of the traction motors that drive them with a Reluctance Synchronous Machine (RSM) along with a general problem statement, the proposed hypothesis and solution formulation as well as a guide to the rest of the dissertation.

1.1 Brief background and general problem statement

A shuttle vehicle is a mobile, traditionally electrically powered vehicle used to transport coal in an underground mine from the continuous miner at the coal face to the primary haulage medium (conveyor belt). It is a critical link in the coal mining process and no coal can be mined if the shuttle vehicle is not available. A typical shuttle vehicle is made up of four motors - a three-phase (3-Φ) pump motor, a 3-Φ conveyor motor and two 3-Φ traction motors [1]. The traction motors are typically interfaced to a traction reducer (gearbox) which is then coupled to the axle to drive the wheels of the shuttle vehicle. Power is delivered to the shuttle vehicle from a 3-Φ trailing cable wound onto a cable reel on-board and sourced from a stationary electrical power centre. The trailing cable is reeled in and out as the shuttle vehicle moves between the continuous miner and conveyor belt [2].

The traction motors that drive underground shuttle vehicles are the primary focus of this research. These motors are subject to harsh operating conditions including steep grades, heavy payloads and high ambient temperatures typical to the mining industry. It is imperative to have the right choice of traction drive and to optimise this drive as this will aid in the optimisation of the overall mining process.

Traditionally, DC machines have been used as the drive of choice for shuttle vehicle traction motors owing to their simple control and exceptional torque capability [1]. In recent years, IMs have become the drive of choice for shuttle vehicles due to the reduction in cost of power electronics and a sufficient understanding of AC motor control [3]. Additionally, the use of AC motor control allows for an increased power density as a result of the smaller AC motor when compared to the DC motor. The *Joy Optidrive*$^{\text{TM}}$ system using an AC Variable Speed Drive (VSD) to drive an IM on a shuttle vehicle is a well known example of this. However, a major problem associated with the use of an IM as the traction motor in a shuttle vehicle is the heat generated from current flowing in the rotor bars. This problem is exacerbated by the fact that it is totally enclosed (for robustness in the harsh mining environment). The only way heat is dissipated from the rotor bars is via radiation. The heat needs to radiate through the air-gap, to the stator core, to the motor housing and then finally to the surrounding environment. This equates to a series of thermal resistances and thus the heat generated by the rotor heat source (the rotor bars) is dissipated slowly to the surrounding environment. This problem is further exaggerated by high loading and sometimes overload conditions at which the shuttle vehicles operates. As a result, the traction motor rating is valid only for a finite amount of time (a duty cycle).

A new type of traction drive, a RSM drive, has the ability to offer performance superior to an IM in a traction application. The RSM does not have any rotor bars like the IM and thus does not suffer from the same heating problems. It uses a stator identical to that of the IM but has a different rotor topology that develops reluctance torque as opposed to the typical armature reaction torque in the IM. The RSM is valid for both constant torque and constant power applications and thus has a wide speed range with associated flux-weakening capability [4]. This makes it an ideal candidate for traction vehicle applications where a wide speed range is required [5]. Despite the favourable characteristics of the RSM drive, it has not yet been adopted in industry to replace the IM on a wide scale. A possible reason for this suggested by Haataja in [6] is that so many factories around the world have geared themselves towards IM manufacturing. Changing the industrial process line is difficult as well as expensive and thus companies have shied away from the RSM and stayed with the well known, robust IM as the dominant industrial solution. This is one of the largest obstacles impeding the adoption of the RSM drive. Historically poor power factor and mechanical strength issues have also attributed to the RSM not yet being adopted in industry on a wide scale in the past.

1.2 General hypothesis and solution formulation

It is important to define any initial assumptions before moving forward with the design of the RSM. The design assumptions are listed below:

- The rated speed of the RSM is the same as the original IM - 1500 rpm. Thus, a 4-pole RSM rotor is assumed.
- The stator of the existing IM will not be changed. Only a RSM rotor design will be pursued and not a combined rotor-stator design.
- Due to ease of manufacturing, a Transversely Laminated (TL) RSM rotor topology will be used.

The primary performance criteria of a traction motor is torque. Included in this criteria is overall torque quality which includes the maximisation of average torque and minimisation of torque ripple. Furthermore, an important aspect that should be evaluated during the RSM design is the mechanical strength of the rotor when trying to maximise overall electromagnetic performance.

The Finite Element Method (FEM) is used as a primary engineering design tool for the design of the RSM rotor. With the advent of powerful hardware capable of performing FEM calculations very quickly it is possible to do the electromagnetic design at component level with FEM directly. The RSM electromagnetic design will be performed in a commercially available FEM software package - FLUX®. Once the electromagnetic design is completed in FLUX®, the mechanical strength of the design is investigated via FEM case studies in ANSYS®. Analysis of all relevant data collected from modelling and design is performed in Octave. These software packages are available for the Machines Research Group (MRG) (part of the School of Electrical and Information Engineering (EIE)) at the University of the Witwatersrand (WITS).

After the RSM rotor has been designed, FEM simulation results of the original IM manufactured by Transvaal Electric (Pty) Ltd (TVE) and the newly designed RSM are compared to verify whether the RSM is a viable alternative solution in a traction vehicle application like an underground shuttle vehicle.

1.3 Dissertation layout

The dissertation is made up of six chapters including the current introductory chapter. The chapter directly following this is a detailed account of RSM fundamentals including a brief history, the analytical model and RSM control topologies. Thereafter the design procedure followed to design the RSM using FEM as an engineering design tool is given. This includes the electromagnetic and mechanical design of the RSM. Once this design is completed, a chapter comparing the FEM simulation results of the designed RSM and original IM is presented. Suggestions for future research on the RSM design are then detailed in a separate chapter. This is followed by a concluding chapter summarising the findings of the research. Appendix A includes an example Python file that is used for the electromagnetic design of the RSM. Appendix B contains the geometric details of the final RSM design. Appendix C contains the technical details of the original IM that is envisaged to be replaced by the RSM design. Finally, Appendix D lists the published work relevant to this dissertation.

Chapter 2

Reluctance Synchronous Machine (RSM) Fundamentals

2.1 VSDs in brushless AC drives

VSD applications have traditionally been dominated by DC technology with their low-cost control electronics, four-quadrant operation and reasonable dynamic performance [3]. The disadvantages of a DC drive are the expensive DC motor, low power to volume ratio (as a result of added components like commutator segments and brushes), considerably higher maintenance requirement and it being a known source of Electromagnetic Interference (EMI). In the past 25 years, when high dynamic performance is required, AC drives have begun to dominate over their DC counterparts [7, 12]. This is as a result of the increased capability of digital hardware to allow for on-line machine parameter estimation and thus increased performance [3].

With regards to AC VSD technology, the Permanent Magnet Synchronous Machine (PMSM) is generally accepted as the ideal drive solution by virtue of its synchronous operation, high efficiency and torque ability [12]. The downside to this drive solution is the cost of magnetic material as well as manufacturing complications [12]. The industry standard IM when run with a VSD requires the use of complicated vector control (as a result of slip) and powerful processing capabilities to perform real time calculations of the IM model to obtain good performance [3]. The absence of slip in the RSM as a result of its inherent synchronous operation allows for a simpler control system [13, 14, 16]. The RSM drive is becoming an increasingly attractive candidate in the brushless AC drive field as an optimised RSM exhibits easy control and high

torque density without the temperature problems suffered by IMs especially at low speeds [9, 17].

2.2 RSM as an industrial solution

In recent years there has been a considerable increase in the demand for controlled drives from industry. Industrial applications requiring constant torque often adopt the PMSM drive owing to it's high torque capability with minimal rotor losses [7]. When constant power operation is required (flux-weakening), the IM drive is commonly adopted since the ability of the PMSM to be flux-weakened is limited in comparison [4]. When constant torque and constant power operation is required the RSM is a viable alternative to both the above mentioned AC drives with good torque density and high speed operation [7, 8]. The RSM has been gaining interest from researchers as a result of this comparable torque and wide speed range, its simple production and assembly process (assuming a TL rotor), minimal rotor losses (cold rotor as a result) and higher efficiency when compared to the widely used and widely accepted IM [4]. The primary performance index of the application in mind (traction vehicle) is torque density [9]. The RSM design will prioritise this performance requirement.

An electrical machine that is commonly associated with the RSM is the Switched Reluctance Machine (SRM) owing to the similar manner in which they develop torque - via reluctance torque. Average torque capability in the PMSM and SRM is normally higher than that of the RSM although torque ripple and associated noise and vibration is considerably larger in the SRM [10–12]. This inherent noise and vibration can largely be overcome by the use of the RSM which uses a typical 3-Φ AC machine stator to allow for a smoother air gap permeance function and thus considerably less torque ripple.

With regards to efficiency, it has been found that the RSM runs much cooler than the IM and thus a higher efficiency is expected with less energy being lost to the surrounding environment [4]. It also has a lighter rotor for a given rotor volume (as a result of no rotor bars) which results in a lower inertia and thus a faster transient response to speed changes [13]. Additionally, the IM drive is often derated as a result of the non-sinusoidal voltages and currents that result when driven by a modern VSD [6, 14]. The harmonics in the non-sinusoidal stator currents induce currents in the rotor cage that do not contribute to average torque and thus heat the

motor more than if it were run with a purely sinusoidal excitation. This phenomenon does not exist in the RSM as it does not contain a rotor cage. The only heat on the RSM rotor is as a result of non-zero rotor iron losses which are present on the IM rotor too. According to [15], the Harmonic Voltage Factor (HVF) as defined by NEMA 30.01.2 and IEC 60034-17 can result in a typical derating of the IM of up to 10% since IMs are not traditionally designed for VSD operation but instead for Direct On-line (DOL) start-up.

2.3 RSM brief history and background

The typical RSM has a typical 3-Φ stator similar and in most cases identical to a typical 3-Φ IM stator. The stator winding is distributed in order to produce as close to a sinusoidal Magneto-motive Force (MMF) wave travelling around the air-gap as possible [4]. In the stator design, all but the first and triplen harmonics are reduced. As is well known, the presence of triplen harmonics in the phase distribution increases the first harmonic amplitude of the rotating MMF wave.

The RSM concept is relatively old with the first introduction being in 1923 by Kostko [12]. The second generation of RSM was in the late 1960s which utilised a segmental rotor construction, otherwise known as a Transversely Laminated (TL) rotor [12]. The third generation of RSM introduced the Axially Laminated Anisotropy (ALA) rotor [12]. As seen in Figure 2.1(a), the ALA rotor has magnetic laminations sandwiched between non-magnetic layers (slot insulation, aluminium, copper, injection moulded plastic). This enables the guiding of flux lines in the D-axis and minimises Q-axis flux from flowing [18]. The stacks (often referred to as *rain gutters*) are connected by pole holders (bolts) to the central part which the shaft is connected to [4]. The TL rotor as shown in Figure 2.1(b) is simple to construct as it uses the traditional punched or laser cut laminations cut in a specific way to obtain the preferred flux paths with tangential webs and radial ribs left to connect the rotor together for mechanical stability [19]. The ALA rotor seems attractive as it allows for a better saliency than the TL rotor but lacks in mechanical strength and ease of construction [19]. The TL rotor is the best suited RSM rotor for industrial manufacturing [20]. The ALA rotor has a higher saliency ratio as a result of Q-axis magnetising inductance in the TL rotor being higher than in the ALA rotor (as a direct result of tangential webs and radial ribs in the TL rotor) [6]. However, the ALA rotor has increased rotor losses and torque ripple as a result of the increased rotor magnetic reaction to stator slot harmonics [21]. Additionally, the TL rotor is

more reliable and stable at high speeds and allows for rotor skewing if secondary effects like torque ripple are to be taken care of [18, 22]. It also allows for lower rotor losses at high speeds owing to no rotor barriers directly on the rotor surface [19].

As revealed in Figures 2.1(a) and 2.1(b) the rotor of the RSM is what sets it apart from other brushless AC machines like the IM, Synchronous Machine (SM) and PMSM. The RSM uses the inherent reluctance difference on the D and Q-axes clearly seen in Figures 2.1(a) and 2.1(b) to develop reluctance torque. Reluctance torque is developed as a result of the known tendency of the rotor to line up along a position of least reluctance [12, 23]. The equiflux plot of a TL RSM shown in Figure 2.2, with the appropriate stator current excitation, reveals graphically how the flux lines that result cause a torque to be developed that would attempt to accelerate the rotor in an anti-clockwise direction trying to align it with the position of least reluctance.

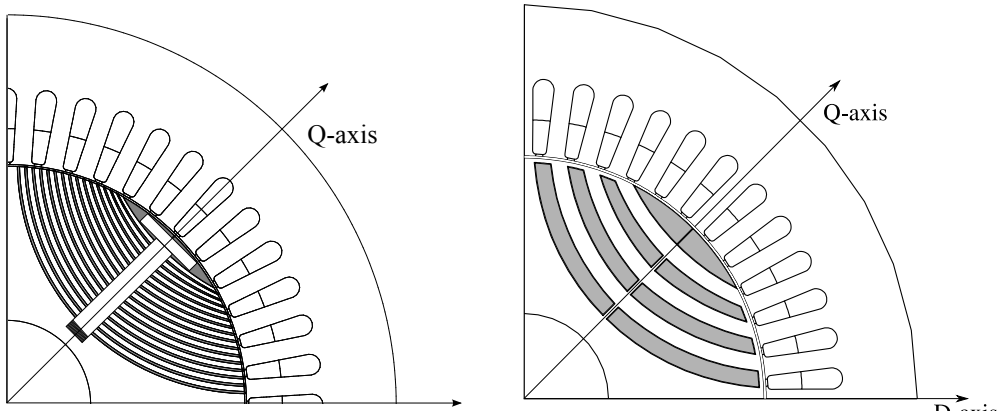
A few industrial solutions of the synchronous IM have also been realised where a typical IM rotor is fabricated but punching or milling of the rotor is performed after fabrication to create saliency [13, 23, 24]. These rotors have been known to have very poor power factors and low saliency ratios. This could be one of the reasons that industry has often shied away from the idea of the RSM in the past.

The performance of line-start RSMs (a RSM with a rotor cage) has been regarded as inferior to other AC machines with regards to power factor, efficiency, pull-out torque and torque density [12, 22, 25]. Also, the RSM with a cage winding means that the advantage it had over the IM with regards to heat from the rotor bars is lost. In recent years, the ability of the RSM to be accurately controlled with a VSD makes the rotor cage or damper winding redundant [18]. This also makes the RSM auto-synchronous (with no concern for pull-out) and the associated control of the RSM can ensure the optimum current angle at all loads and speeds [26].

2.4 Analytical model

In order to obtain a sufficient understanding of the operation of the RSM the well known analytical model will be presented [26, 27]. Using the equivalent circuits in Figure 2.3(a) and Figure 2.3(b) the equations modelling the RSM are presented:

$$V_{ds} = R_s i_{ds} + L_{s\sigma}\frac{di_{ds}}{dt} - \omega\lambda_{qs} + \frac{d\lambda_{dm}}{dt} \tag{2.1}$$



(a) One pole of a typical ALA rotor (b) One pole of a typical TL rotor

Figure 2.1: Two fundamental rotor topologies for RSMs with 4-pole rotors

$$V_{qs} = R_s i_{qs} + L_{s\sigma}\frac{di_{qs}}{dt} + \omega\lambda_{ds} + \frac{d\lambda_{qm}}{dt} \tag{2.2}$$

$$i_{ds} = i_{dm} + \frac{1}{R_m}[-\omega\lambda_{qs} + \frac{d\lambda_{dm}}{dt}] \tag{2.3}$$

$$i_{qs} = i_{qm} + \frac{1}{R_m}[\omega\lambda_{ds} + \frac{d\lambda_{qm}}{dt}] \tag{2.4}$$

where

V_{ds} = Stator voltage in the D-axis
V_{qs} = Stator voltage in the Q-axis
i_{ds} = Stator terminal current in the D-axis
i_{qs} = Stator terminal current in the Q-axis
i_{dm} = D-axis magnetising current
i_{qm} = Q-axis magnetising current
λ_{ds} = D-axis stator flux linkage
λ_{qs} = Q-axis stator flux linkage
λ_{dm} = D-axis magnetising flux linkage
λ_{qm} = Q-axis magnetising flux linkage
R_s = Stator per phase resistance
R_m = Equivalent iron loss resistance
$L_{s\sigma}$ = Stator per phase leakage inductance
ω = Electrical angular velocity

The flux linkages and electromagnetic torque can be expanded upon as:

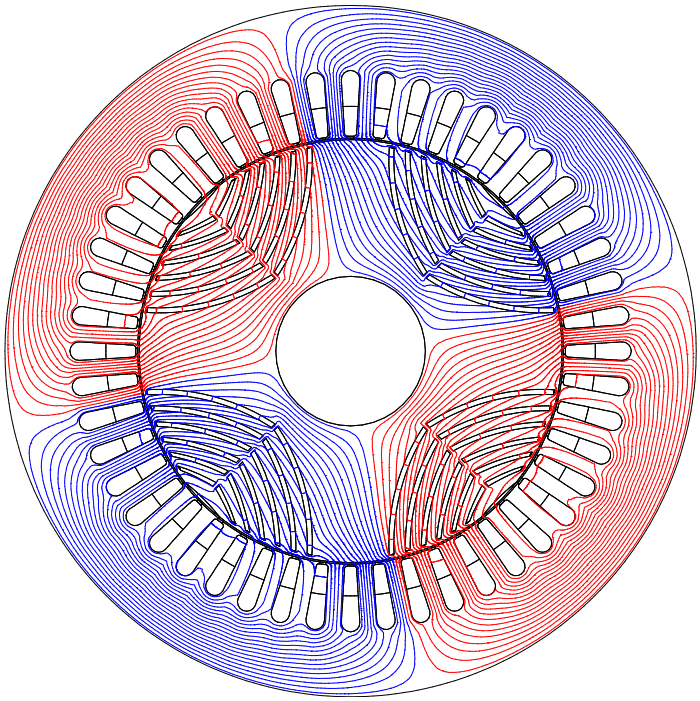


Figure 2.2: Equiflux plot of RSM illustrating reluctance torque

$$\lambda_{ds} = L_{s\sigma} i_{ds} + \lambda_{dm} \tag{2.5}$$

$$\lambda_{qs} = L_{s\sigma} i_{qs} + \lambda_{qm} \tag{2.6}$$

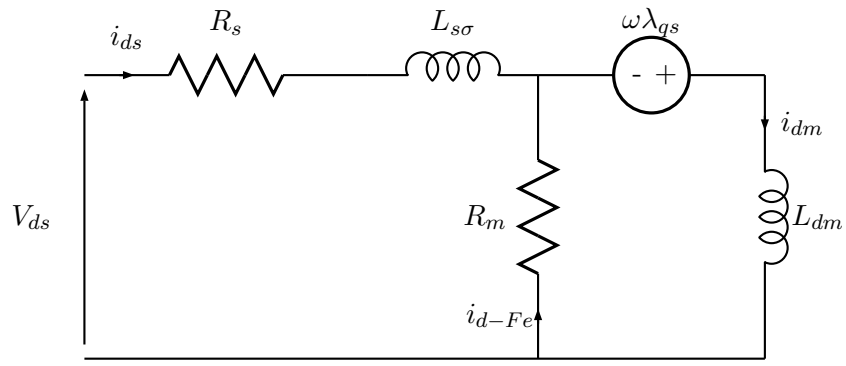
$$\lambda_{dm} = L_{dm} i_{dm} \tag{2.7}$$

$$\lambda_{qm} = L_{qm} i_{qm} \tag{2.8}$$

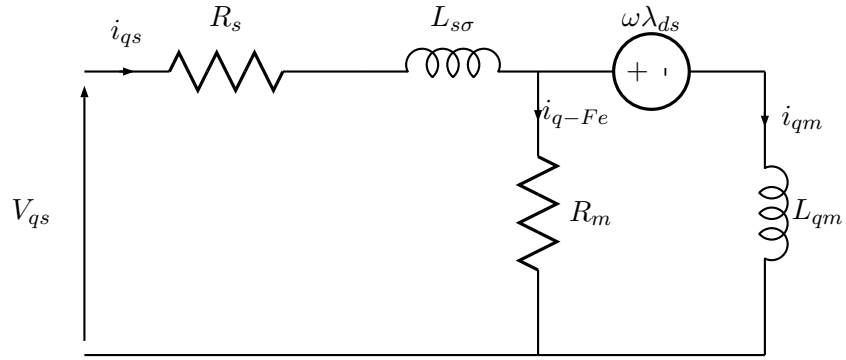
$$T_{el} = \frac{3P}{2}(\lambda_{ds} i_{qm} - \lambda_{qs} i_{dm}) \tag{2.9}$$

where

L_{dm} = D-axis magnetising inductance
L_{qm} = Q-axis magnetising inductance
T_{el} = Electromagnetic torque
P = Number of pole pairs in the machine



(a) D-axis model of RSM



(b) Q-axis model of RSM

Figure 2.3: D and Q-axis equivalent circuits of RSM

The relation between the terminal current space vector i_{dqs} and the magnetising current space vector i_{dqm} is shown in Figure 2.4. As the core loss resistance R_m approaches infinity (core losses are disregarded) the two current space vectors (i_{dqs} and i_{dqm}) become identical. By considering equation 2.9 and Figure 2.4 the electromagnetic torque can be interpreted as the interaction between the stator flux linkage space vector λ_{dqs} and the magnetising current space vector i_{dqm}. It should be noted that the terminal current space vector i_{dqs} as seen from the terminals of the RSM is not the current vector that directly governs torque development. Instead, the current space vector i_{dqm} (which lags the terminal current space vector i_{dqs}) along with the stator flux linkage space vector λ_{dqs} directly govern torque production.

The coupling between the electromagnetic system (detailed in equations 2.1-2.9) and the mechanical system is made in [28] by the following:

$$T_{el} = T_{mech} + \frac{J_{eq}}{P}\frac{d\omega}{dt} + \frac{B_{eq}}{P}\omega \tag{2.10}$$

where

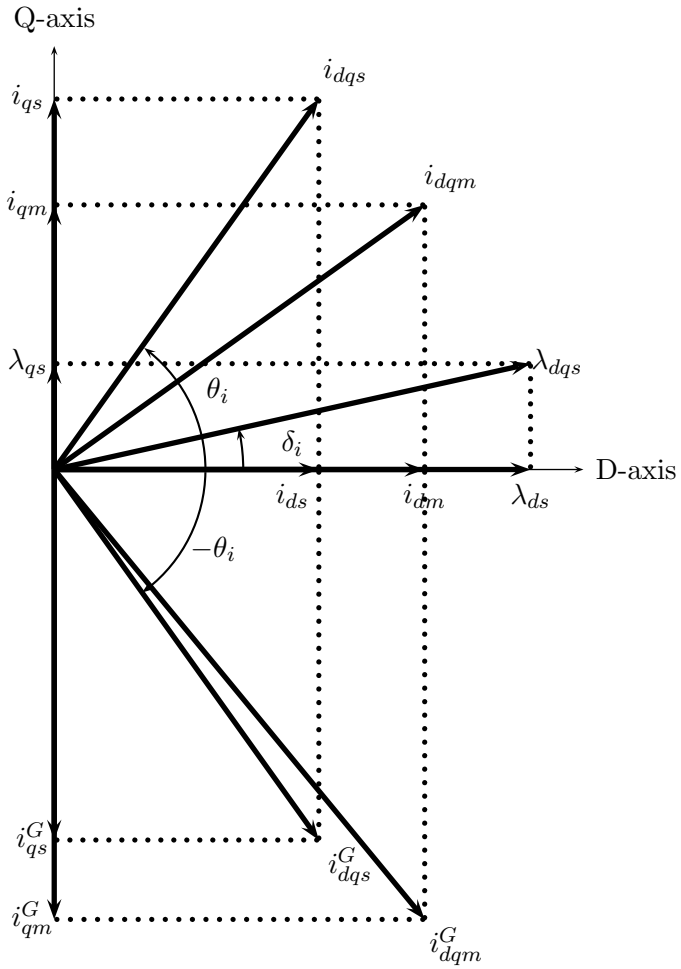


Figure 2.4: Phasor diagram of RSM including iron losses

T_{mech} = Mechanical load torque
J_{eq} = Combined moment of inertia of machine and load
B_{eq} = Combined friction coefficient of machine and load

Under full-load, most RSMs become magnetically saturated as a result of the combined effect of saturation predominantly in the rotor mechanical supports and stator teeth [18]. This saturation causes a magnetising inductance variation in both the D and Q-axes (exaggerated in the D-axis). This causes discrepancies between the RSM model and the actual machine [29]. Even if a linear model is not assumed, it is difficult to estimate the saturation characteristic without actual measurements on the real machine. Saturation predominantly occurs on the D-axis as a result of the magnetic path being predominantly iron [4, 25]. There is very little saturation on the Q-axis as a result of the magnetic path being predominantly air [4, 25]. Thus, the relation between λ_{qs} and i_{qm} (which determines L_{qm}) is often approximated by a linear one [4], meaning L_{qm} can typically be considered approximately constant under all loading conditions. The D-axis saturation is taken into account via the

non-linear relation between λ_{ds} and i_{dm}. This means that L_{dm} is not constant but rather a state dependant variable that can easily decrease at rated or above rated conditions [18]. The differences in saturation characteristics on the D and Q-axes makes control of the respective currents more complex [26]. In addition to this, cross-coupling between the D and Q-axes can occur and this can further complicate control accuracy. The effect of cross-saturation is ignored for this dissertation but the phenomenon has been dealt with extensively [6, 30].

The magnetising saliency ratio, which excludes leakage inductance $L_{s\sigma}$, is defined in [12] as:

$$\xi_m = \frac{L_{dm}}{L_{qm}} \tag{2.11}$$

where

ξ_m = Magnetising saliency ratio

As has been shown [16, 18], an increased saliency ratio results in increased overall performance of the RSM. The true saliency ratio of the RSM should include the swamping term that leakage inductance adds [13]:

$$\xi = \frac{L_{dm} + L_{s\sigma}}{L_{qm} + L_{s\sigma}} \tag{2.12}$$

where

ξ = True saliency ratio

Another characteristic value closely related to the saliency ratio ξ is the torque index ζ. The torque index ζ is defined as:

$$\zeta = L_{dm} - L_{qm} \tag{2.13}$$

This is an important parameter as maximising it will allow for maximum torque density in the RSM. This can be realised by considering equation 2.9 and simplifying the model by assuming zero iron losses and neglecting stator leakage inductance. This will result in the following:

$$T_{el} = \frac{3P}{2}\zeta i_{ds} i_{qs} \tag{2.14}$$

Alternatively, using simple trigonometry as:

$$T_{el} = \frac{3P}{4}\zeta i_{dqs}^2 sin(2\theta_i) \tag{2.15}$$

It can be seen from equation 2.14 and 2.15 that if a constant current space vector i_{dqs} with associated constant current angle θ_i was driving the RSM, the only parameter defining the torque capability is the torque index ζ. The higher the torque index the higher the torque capability of the RSM.

2.5 Control fundamentals

Although control of the RSM is not the primary focus of this dissertation, a specific control type is used during the RSM design presented in chapter 3 and thus a basic understanding of how a typical RSM is controlled is presented. A well designed RSM rotor with a poor control system will never result in the desired performance for the end application.

2.5.1 Ideal RSM control

The RSM is current controlled in order to obtain torque control [4]. Vector control of the D and Q-axis currents is a mature technique in AC drives and it allows for controller simplicity and inherent inverter protection in the form of current limiting [4, 18]. With the control of the RSM in the rotor DQ reference frame there is an obvious requirement for the commanded D and Q-axis currents to be transformed back onto the stationary reference frame and into meaningful 3-Φ quantities. This requires rotor position information in the form of optical encoders or magnetic resolvers in order to perform the required transformations. Any angular errors introduced by these devices can negatively affect control as the required current space vector will not be realised. A constant angular offset could be present due to resolver/encoder assembly, the demodulation of resolver signals could introduce angular errors proportional to speed and angular ripple could be introduced dependant on angular position [4]. Thus, it should be kept in mind that the detection of rotor angle via optical encoders or magnetic resolvers is a possible source of inaccuracy and even robustness in the RSM control system. This is the

primary reason for researchers pursuing sensorless control of the RSM in recent years [29, 31–33].

The main control parameter in the control of a RSM is the current space vector angle θ_i as shown in Figure 2.4 and contextualised in the ideal case of equation 2.15 where iron losses are ignored. In this ideal case where iron losses are neglected and no saturation is considered, there exists the following well known control topologies [18]:

- Maximum Torque Control (MTC); $\theta_i = \frac{\pi}{4}$.
- Maximum Rate of Change of Torque Control (MRCTC); $\theta_i = \tan^{-1}(\xi)$.
- Maximum Power Factor Control (MPFC); $\theta_i = \tan^{-1}(\sqrt{\xi})$
- Maximum Efficiency Control (MEC); $\theta_i = \frac{\pi}{4}$.
- Constant Current in Inductive Axis Control (CCIAC); Constant current in the D-axis is maintained and torque is changed by varying Q-axis current.

It has been shown by Betz et al. in [18] that at lower speeds, CCIAC is superior to the Constant Angle Control (CAC) topologies listed (MTC, MRCTC, MPFC, MEC) with regards to rate of change of torque but at higher speeds the CAC topologies are superior to CCIAC. In order to optimise the overall RSM drive in the widest range possible, investigations have been performed into the possibility of shifting from one control topology to the other when it seems feasible (if better performance will be attained) [34]. The difficulty in this is a smooth transfer from CAC to CCIAC and vice-versa. Conceptually, the switch from CCIAC to CAC can be made when a certain performance criteria, like the rate of change of torque, in the CAC is greater than the rate of change of torque in the CCIAC [34].

2.5.2 Parameter effects on RSM control

From the control topologies listed in section 2.5.1 it is clear that there exists a sensitivity of the control schemes to errors in saliency ratio ξ. Thus, it is important to have a good estimation of L_{dm} and L_{qm} in order to make sure the correct current angle θ_i is chosen to result in the relevant control outcome [18, 34]. The inductances L_{dm} and L_{qm} can be determined off-line and stored in Look-Up Tables (LUTs) or their estimation can be performed online [18, 30]. The latter allows

for decoupling between the controller and machine and thus the controller can be used on any other RSM with a similar power rating. The sensitivity of performance to errors in the determination of the inductances has been investigated in [34] and in most cases performance degrades if L_{dm} and L_{qm} are not correctly estimated.

For on-line parameter estimation, most estimation schemes use the basic Recursive Least of Squares Estimator (RLSE) [34]. In the RLSE, an error is constructed from the difference between a feedback quantity i_{ds} and an estimated value of this parameter i^*_{ds} generated from the RSM parameters being estimated [34]. This error is then used to drive a RLSE to update the estimated parameter values of interest.

In the work by Niazi in [30], the parameter estimator has D and Q-axis stator currents as well as speed fed to it to determine estimates of the inductances. These estimates are fed to a maximum torque per ampere controller along with a reference current magnitude from an outer speed loop. The controller then decides on the relevant values of D and Q-axis currents required to obtain maximum torque. This is based on a small perturbation of the current angle θ_i to find where maximum torque (for the specified current magnitude) will occur. The controller outputs are reference D and Q-axis voltages. These reference voltages are then synthesised into the required three phase voltages via Space Vector Modulation (SVM).

2.5.3 Effects of iron loss and saturation

Ideally, as the RSM rotor rotates synchronously with the main (fundamental) flux waveform, the rotor sees a DC flux and thus no frequency modulation is seen by the rotor. However, with the interaction of stator slots and rotor barriers, higher frequency asynchronous waves rotate at a different speed to the main flux and thus rotor losses are induced [18, 19, 26]. If the stator slots are semi-closed and rotor barrier placement properly designed, these losses can be confined to the rotor surface and thus kept fairly small [35].

The stator winding losses in the RSM are proportional to the square of the stator current and the core losses proportional to the square of the back Electromotive Force (EMF) in each axis. At lower speeds, RSM losses are dominated by winding losses and at higher speeds core losses become dominant [36]. These two loss mechanisms are often overlooked when analysing RSM performance and control. However, it is important to consider them as the effect that iron loss especially has on the control of the RSM (especially at high speeds) cannot be neglected if optimum performance

is desired [4, 19]

Accurately modelling iron loss is a complex task involving non-linear and distributed parameter phenomena [4]. More specifically, the calculation of iron losses requires the knowledge of the flux density at individual locations in the machine [37]. The study performed in [37] found that losses were induced in the rotor as a result of the pulsating nature of the permeance air-gap function changing for different rotor positions. In [38], core losses are accounted for from the air-gap flux density waveform. The associated power losses were calculated for different excitation frequencies based on manufacturer data and the air-gap flux density waveform. It was found that FEM results closely resembled measured laboratory results whereas analytical solutions deviate significantly. This reveals the clear advantage that FEM has over the traditional analytical and empirical methods to accurately model complex phenomena and thus have better control of the RSM.

The classical RSM control topologies introduced in sub-section 2.5.1 have current angle choices θ_i that do not account for iron losses and saturation. If these two phenomena were accounted for, the resulting expressions for current angle θ_i for the different control strategies would change. The expressions become very complex functions of the motor parameters. In the following, general effects on θ_i are noted instead of introducing these complex relations:

- MTC:
  - When considering the effect of saturation, the non-linear relation between λ_{ds} and i_{dm} is taken into account [7]. The choice of the terminal current space vector i_{dqs} that results in the magnetising current space vector i_{dqm} should be made so that the iron does not saturate significantly [18, 26]. Also, iron loss is dependant on operating frequency due to the speed voltage terms in the RSM model shown in Figure 2.3(a) and Figure 2.3(b). If frequency is higher, the current through R_m is larger and thus core losses are larger. As a result, the choice of current angle θ_i would be higher in order to allow for the magnetising current space vector i_{dqm} to have an angle with the D-axis that allows for maximum torque per ampere.
  - A current angle range of $55^o \geq \theta_i \geq 65^o$ is quite suitable for MTC [22].
- MRCTC

  - The large current angle chosen for this control topology also results in little saturation in the D-axis and thus the effects of saturation are not noticed. Thus, the deviation of θ_i from the ideal value is minimal [18, 27].
  - Values of the current angle are typically around $\theta_i = 80^o$ without considering the effects of saturation and iron loss. When including iron loss and saturation a slightly larger current angle is typically chosen.

- MPFC
  - The current angle chosen in this topology does not vary considerably from the value under ideal conditions nor does it vary considerably for different loads [27]. Essentially, the large current angle that is chosen in this type of RSM control results in little saturation in the D-axis and thus the effects of saturation are not noticed.
  - A current angle slightly higher than the ideal case should be chosen as a result of the effect that iron loss has on the terminal current space vector.

- MEC
  - The choice of current angle for MEC is a function of the operational speed [39]. This can be understood by considering the two dominant loss mechanisms in the RSM - copper losses and core losses. Copper losses remain essentially constant for a defined load but core losses increase as a function of speed as a result of more current being pushed through resistor R_m via the EMF sources in the equivalent circuits. At lower speeds, MEC approaches the MTC topology and at higher speeds MEC approaches the MRCTC topology [39].
  - A specific torque at any operating point (speed) can be achieved with a variety of i_{ds} and i_{qs} combinations but overall efficiency would vary widely [40]. Intuitively, there exists a combination of i_{ds} and i_{qs} at any torque and operating speed that would yield optimum efficiency (minimum copper and core losses) [39]. This optimum efficiency is acquired by measuring the input power and perturbing i_{ds} to seek where input power is minimised for that particular operating point [40]. This is similar to the control algorithm adopted by Niazi in [30].
  - Saturation and iron loss have a significant effect on current angle choice. Current angle values in the range of $75^o \geq \theta_i \geq 80^o$ are typical [18].

Generally speaking, when saturation and iron loss is accounted for, the current angle θ_i chosen for the relevant control strategy is typically a function of operating

speed and is chosen to be sufficiently large so as to avoid saturation in the D-axis, especially at higher loads [27].

2.6 Summary

In many industrial applications (including traction vehicles) DC machines have been replaced by Induction Machines (IMs), even though IMs have disadvantages including a hot rotor and relatively complex control algorithms. The Reluctance Synchronous Machine (RSM) is suggested as a new traction vehicle industrial drive as a result of its comparable torque performance, easy control and cooler steady state operating temperature. The two most commonly used RSM topologies are the Transversely Laminated (TL) and Axially Laminated Anisotropy (ALA) rotors. The ALA rotor traditionally presents better electromagnetic performance but is more difficult to manufacture and lacks mechanical strength.

A model of the RSM is presented in the form of detailed equivalent circuits and analytical equations. The model provides an essential foundation for the understanding of the fundamental operation of the RSM. An important result from the analytical model is that a higher saliency ratio ξ and torque index ζ will allow for better performance especially with regards to torque production.

Control of the RSM requires accurate control of the current space vector angle θ_i to obtain a specific control goal. The well known control schemes include Maximum Torque Control (MTC), Maximum Rate of Change of Torque Control (MRCTC), Maximum Power Factor Control (MPFC), Maximum Efficiency Control (MEC) and Constant Current in Inductive Axis Control (CCIAC). The choice of control scheme can be made based on loading and speed as a result of the control schemes delivering better performance at different operating points. The variation of machine parameters can degrade control performance as accurate control is often dependant on parameter estimation. Furthermore, there is a large difference in the resultant current angle choice in most of the control schemes if iron losses and saturation are taken into account.

Chapter 3

RSM Finite Element Modelling and Design Procedure

3.1 FEM background

A working knowledge of the Finite Element Method (FEM) is essential before the design of the RSM is presented. In the sections that follow, the aim is not to teach FEM but rather to provide a basic background on FEM and its application in electrical machine analysis. If a more thorough treatment of the topic is required good references are available [41–44].

3.1.1 Basics of FEM

FEM is a numerical technique which uses a *divide and conquer* approach to solve a spatial problem. It takes a large problem space and breaks it down into a number of smaller problems called finite elements (via the use of meshing). A meshed domain traditionally consists of triangular elements with vertices called nodes. An example of this is shown in Figure 3.1. The first emergence of FEM in engineering was in the 1940s but it was only applied ten years years later for the first time in aeronautical design and structural analysis [41]. The analysis when using FEM is distributed in space and thus the required computation time is considerable especially when a large number of finite elements are defined. Digital hardware that is required to run FEM simulations needs to be quite powerful in order to reduce simulation time. In recent years, increased hardware ability has resulted in a significant increase in the use of FEM in the design and analysis of electromagnetic devices (including

electrical machines). It has become a widely accepted machine design tool and has the advantage of taking into account distributed electromagnetic phenomena like magnetic saturation, leakage flux, iron losses and cross-magnetisation [6]. Aspects of machine design that were previously accounted for via analytical methods and empirical formulae can now be taken into account accurately via the use of numerical methods like FEM.

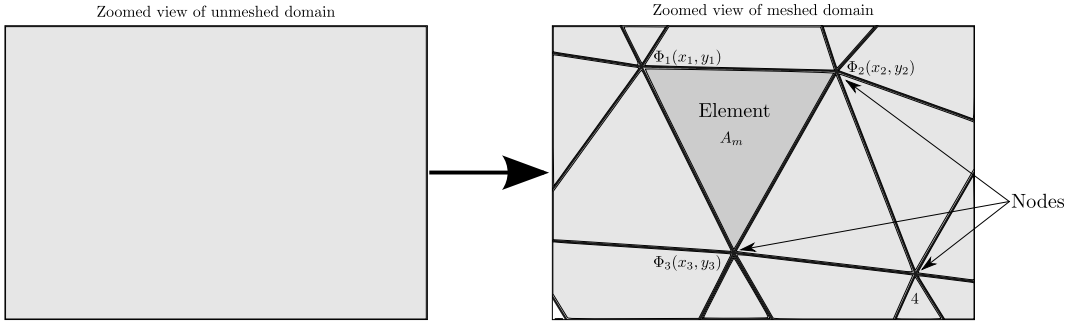


Figure 3.1: Example mesh with four nodes and one complete element

3.1.2 Electromagnetic application of FEM

When using FEM in the study of electromagnetic devices, the distribution of the electric and magnetic fields in the structure under study are determined [41]. The magnetic and electric vector fields are computed by starting with the well known fundamental vector field equations developed by Maxwell:

$$\text{curl}\mathbf{H} = \mathbf{J} + \frac{\partial \mathbf{D}}{\partial t} \tag{3.1}$$

$$\text{curl}\mathbf{E} = -\frac{\partial \mathbf{B}}{\partial t} \tag{3.2}$$

$$\text{div}\mathbf{B} = 0 \tag{3.3}$$

$$\text{div}\mathbf{D} = \rho \tag{3.4}$$

where

$\mathbf{H}$ = Magnetic field strength
$\mathbf{J}$ = Current density
$\mathbf{D}$ = Electric field displacement
$\mathbf{E}$ = Maxwell's electric field (sum of the Coulomb and induced field)
$\mathbf{B}$ = Magnetic flux density
ρ = Density of electric charge

All the vector fields given in equations 3.1-3.4 can be dependant on position and time. The constitutive relationships in equations 3.5-3.7 along with the continuity equation 3.8 for the vector fields are:

$$\mathbf{B} = \mu\mathbf{H} \tag{3.5}$$

$$\mathbf{D} = \epsilon\mathbf{E} \tag{3.6}$$

$$\mathbf{J} = \sigma\mathbf{E} \tag{3.7}$$

$$\text{div}\mathbf{J} = -\frac{\partial\rho}{\partial t} \tag{3.8}$$

where

μ = Magnetic permeability
ϵ = Electric permittivity
σ = Electric conductivity

One of the biggest advantages of using FEM is that the defined materials can be non-homogeneous and non-linear. A non-homogeneous material has co-efficients μ, ϵ and σ that are different in each axis and at each position in the defined space. A materials' non-linear behaviour is accounted for by the same co-efficients. When a material is non-linear, the co-efficients become a function of the magnetic field or electric field. In other words, the magnetic permeability becomes a function of $\mathbf{H}$ (so that saturation can be accounted for) and ϵ and σ become functions of Maxwell's electric field $\mathbf{E}$.

To determine a unique solution of the geometry, the relevant boundary conditions of the FEM problem space should be defined. Boundary conditions define the

value of the magnetic vector potentials on the boundaries of the geometry. There are typically two types of boundary conditions - the Dirichlet's condition and the Neumann's condition [41]. The Dirichlet's boundary condition sets the value of the magnetic vector potential on the boundary of interest equal to a constant value. A common Dirichlet's condition is the homogeneous Dirichlet's condition. The homogeneous Dirichlet's condition sets the value of the magnetic vector potential on the chosen boundary to zero. In this condition, the flux lines run parallel to the boundary and no flux lines cross the boundary. A Neumann's condition corresponds to the derivative of the magnetic vector potential being given a specific value at the boundary of interest. A homogeneous Neumann's boundary condition has the derivative of the magnetic vector potential set equal to zero. This essentially means that the flux lines are forced to be perpendicular to the boundary of interest.

3.1.3 Magnetostatic field problem

A magnetostatic application as detailed in [41] is expanded upon in the following. By using the equations given in section 3.1.2 the magnetostatic application can be defined by the following:

$$\text{curl}\mathbf{H} = \mathbf{J} \tag{3.9}$$

$$\text{div}\mathbf{B} = 0 \tag{3.10}$$

$$\mathbf{B} = \mu\mathbf{H} \tag{3.11}$$

The vector fields in equations 3.9-3.11 are not time dependant as a result of the application being static. A magnetic vector potential $\mathbf{A}$ can be defined:

$$\mathbf{B} = \text{curl}\mathbf{A} \tag{3.12}$$

Thus, the field problem is taken from equations 3.9, 3.11 and 3.12 and is defined as:

$$\text{curl}\mathbf{H} = \text{curl}\frac{\mathbf{B}}{\mu} = \text{curl}\frac{1}{\mu}\text{curl}\mathbf{A} = \mathbf{J} \tag{3.13}$$

If a 2-dimensional (2-D) geometry is assumed, the current density **J** has only a z-axis component $\mathbf{J} = [0, 0, J_z]$. The magnetic vector potential **A** is parallel to the current density vector **J** and thus also only has a z-axis component $\mathbf{A} = [0, 0, A_z]$. Taking these simplifications into account and assuming a homogeneous material ($\mu_x = \mu_y = \mu$), equation 3.13 is expressed as a Poisson's equation:

$$\frac{\partial^2 A_z}{\partial x^2} + \frac{\partial^2 A_z}{\partial y^2} = -\mu J_z \tag{3.14}$$

With the imposed current density at the relevant positions in the defined space, the solution to the differential equation in equation 3.14 is found. The current density is the source (as defined by the user) and the magnetic vector potential is the unknown. It must be noted that the magnetic permeability μ can define the non-linear nature of a material in the geometry and is dependant on the magnetic field intensity which is in turn dependant on the current excitation level. Once equation 3.14 is solved (the magnetic vector potential is known at each node), a typical linear interpolation of this potential in each element of the geometry is used so that the potential at any point in the geometry can be determined.

Quantities of interest like the flux density and magnetic field strength are derived from the solved magnetic potential at each node in the geometry. Also, the magnetic forces that act on an object in the geometry can be calculated by the Maxwell stress tensor or the virtual work principle [41]. In the Maxwell stress tensor method, a line that encloses the object of interest is defined and the two components of force calculated using the relevant components of the magnetic field (normal and tangential). Maxwell's stress tensor method only requires one field computation. This is in contrast to the virtual work method which inherently requires two field computations. The virtual work method calculates the force of interest by calculating the change in magnetic co-energy with respect to a change in position of the object of interest while maintaining the same excitation [45].

3.2 RSM electromagnetic design

3.2.1 Background

When the electrical machine designer is interested in accurate non-linear magnetic behaviour as well as fringing effects, overloading and flux path deviations from the

ideal well known analytical magnetic circuit models (presented in chapter 2), a design should be performed using FEM. It should be noted that although the application of the RSM design presented is an underground shuttle vehicle, the design procedure results in a RSM rotor that can be used in any traction vehicle application. This is as a result of maximum torque being the primary design criteria and any traction vehicle requires this maximum torque density.

The geometric parameters that will be optimised in the RSM rotor design are shown in Figure 3.2 and briefly summarised in Table 3.1. The mechanical strutting parameters l_{rr} (length of the radial ribs) and l_{tw} (length of the tangential webs) are not optimised electromagnetically since optimum electromagnetic performance is attained when these values are zero. However, this is contradictory to mechanical requirements as the rotor would have no way of holding itself together and would disintegrate. Thus, l_{tw} and l_{rr} need to be non-zero and are changed purely for investigative purposes in the electromagnetic design procedure. The mechanical design detailed in section 3.3 will determine the appropriate widths of these supports.

Table 3.1: Parameters to be changed during electromagnetic design procedure.

Parameter	**Description**
N_{rb}	Number of rotor barriers
$\beta = \frac{b_{bw}}{b_{bw} + b_{lw}}$	Rotor insulation ratio
W_p	Position of first rotor barrier
$\alpha = \frac{\tau}{\tau_p}$	Pole pitch to pole span ratio
g	Air-gap length

3.2.2 Hardware and software requirements

In order to run the relevant FEM simulations, a workstation with sufficient computing power is required to minimise computation time. The MRG currently uses a

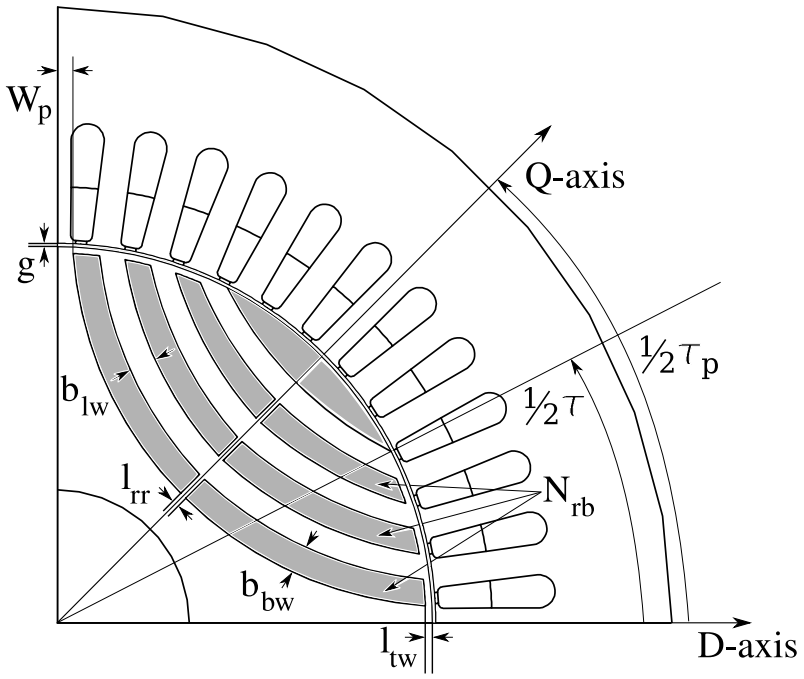


Figure 3.2: Geometric parameters of a TL RSM rotor

workstation running Windows Server 2003 standard x64 Edition with Service Pack 2 installed. The workstation has a 3.10 GHz Intel Core 2 Quad Q9300 processor with a 64 KB memory cache. In order to do quick FEM calculations a significant amount of RAM is required. The workstation has 4 GB of installed RAM. For display purposes, an NVIDIA GeForce 7300 GS is installed. FEM simulations are performed on the workstation via a remote desktop connection. This allows for the many users within the research group to work with the same workstation simultaneously.

In terms of software requirements, two software packages are used. For the electromagnetic FEM design procedure, FLUX® from Cedrat is used. Extensive post-processing and data handling is carried out in Octave.

3.2.3 Electromagnetic design procedure

In order to design the RSM rotor, the most important performance criteria for the application should be prioritised. In this design, the traction motor end application requires torque density to be prioritised [9]. The torque requirement should not only be the maximisation of average torque but should also include the minimisation of torque ripple. Thus, the rotor is rotated through a predefined angle with a

specified excitation and torque determined at each angular position. An example of a full torque waveform is shown in Figure 3.3(a). From this, it can be seen that the torque waveform repeats itself every 30^o and thus there are 12 peaks per revolution. This result is very advantageous as the number of FEM calculations can be reduced substantially. During the design, the rotor is rotated by 30^o as shown in Figure 3.3(b) to fully account for the torque ripple. The rotation of the rotor is done with a constant chosen current vector angle of $\theta_i = 60^o$ to allow for as close to MTC as possible [20, 28]. The torque at each rotor position is calculated in FLUX® via the virtual work principle. The method used to extract average torque and torque ripple has been used by a number of other authors [6, 30, 46]. The mean electromagnetic torque and torque ripple as defined graphically in Figure 3.3 are defined mathematically as:

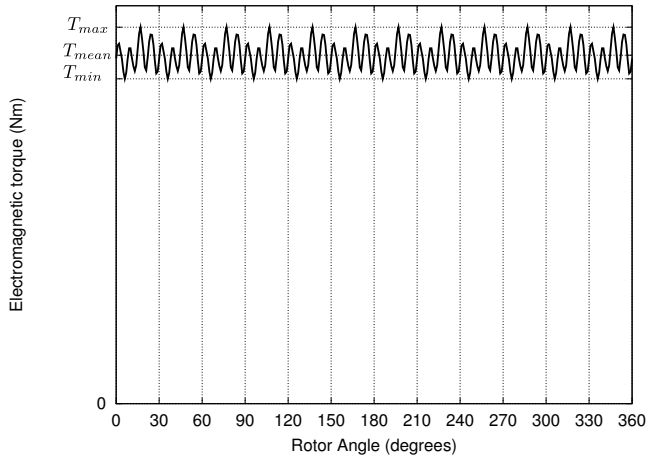
$$T_{mean} = \frac{\sum_{a=0}^{N} T_{ea}}{N} \tag{3.15}$$

$$T_{ripple} = \frac{T_{max} - T_{min}}{T_{mean}} \times 100\% \tag{3.16}$$

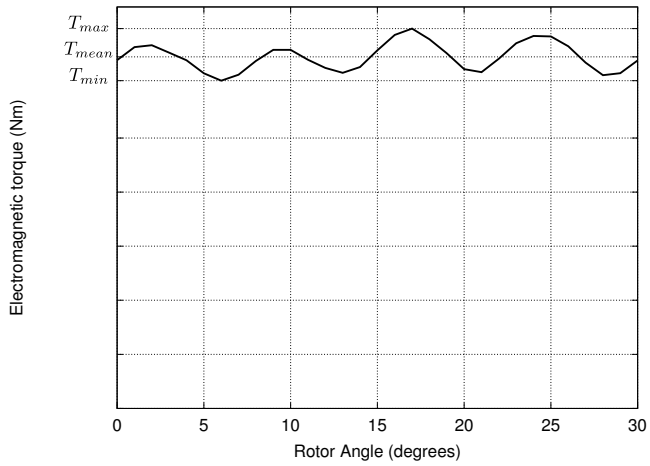
where

T_{mean} = Mean torque of torque waveform
a = a_{th} element in torque waveform
T_{ea} = Value of torque at the a_{th} position in torque waveform
N = Total number of elements in torque waveform
T_{max} = Maximum torque in torque waveform
T_{min} = Minimum torque in torque waveform
T_{ripple} = Calculated torque ripple

The overall electromagnetic design procedure follows the flow diagram in Figure 3.4. It investigates the geometric parameters effect on torque production in a linear progression. This is not an optimum global multi-variable design but a design to investigate the effects that the parameters listed in Table 3.1 have on average torque and torque ripple. In the design, one parameter is varied and the torque waveform analysed over the defined rotor angle. The mean torque and torque ripple are then determined using equations 3.15 and 3.16. Thereafter, the parameter value which results in maximum average torque and minimum torque ripple is normally chosen. This value of the relevant parameter is then utilised for the rest of the design procedure that follows where the process is repeated until all parameter values have been chosen accordingly. The order in which the design proceeds is the number of



(a) Torque waveform for a full rotation



(b) One period of the torque waveform

Figure 3.3: Example torque waveforms as a function of rotor angle

rotor barriers (N_{rb}) and insulation ratio (β) together, the position of the first rotor barrier from the D-axis (W_p), the pole pitch to pole span ratio (α) and finally the length of the air-gap (g).

3.2.4 Electromagnetic design implementation in FLUX®

The electromagnetic design is implemented using Python scripts incorporating generic Python and the built in PyFLUX command language in FLUX®. The use of the FLUX® 3-dimensional (3-D) beta solver allows for all required model development, solving and post-processing to be incorporated into one integrated development environment. This also allows for insight into the relevant PyFLUX commands required for solving and post-processing. The geometry of the RSM is developed

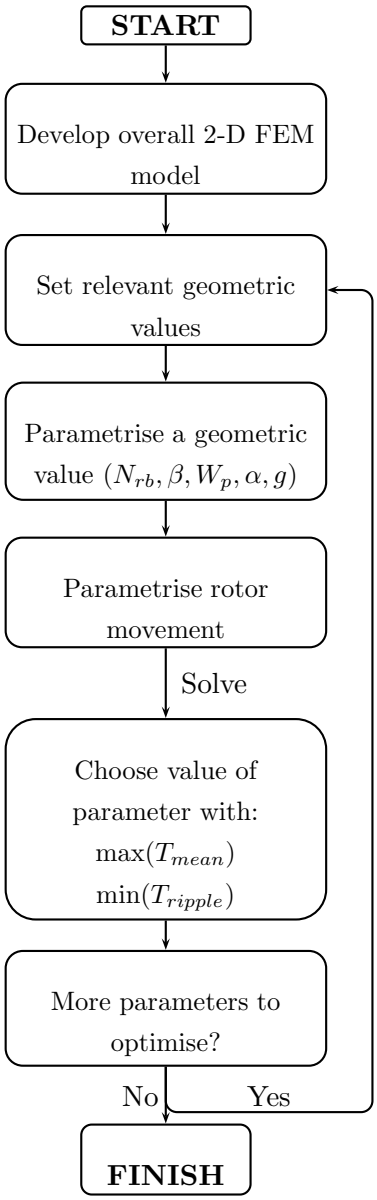


Figure 3.4: Linear progression approach for design procedure

parametrically to allow for quick changes when required. The three stator windings have two parallel paths. Each of the relevant coil conductor areas in the geometry are assigned as stranded coil conductors with the relevant number of turns and imposed currents defined by three I/O parameters as follows:

$$I_a = I_p \sin((2\theta + \theta_i)\frac{\pi}{180}) \tag{3.17}$$

$$I_b = I_p \sin((2\theta + \theta_i)\frac{\pi}{180} + \frac{2\pi}{3}) \tag{3.18}$$

$$I_c = I_p \sin((2\theta + \theta_i)\frac{\pi}{180} - \frac{2\pi}{3}) \tag{3.19}$$

where

I_{rated} = Rated current of original induction machine

I_p = IM and RSM individual stator winding peak current = $\frac{I_{rated}}{2}\sqrt{2}$

The rated current $I_{rated} = 93\ A$. The peak current is half the typical value as a result of the stator windings being made up of two parallel paths. The reason for the double rotor angle argument in the three phase currents is because the stator is designed for four-pole operation and thus the rotor angle needs to be converted to an electrical value. The current angle θ_i included in the three phase currents will set the current space vector angle from the D-axis ($\theta_i = 60^o$). The stator and rotor are assumed to be homogeneous but non-linear and are assigned as M400-50A steel. The shaft is assumed non-magnetic (vacuum) and the rotor barriers are assigned as a vacuum. An active core depth of 325 mm is used. The boundary condition of the geometry is defined as a homogeneous Dirichlet's boundary condition on the outer stator periphery.

The RSM problem is solved in a magnetostatic application as it allows for quick computation time and reasonable results. The use of a magnetostatic solver for the design of the RSM rotor has previously shown promising results [6, 21, 30].

Separate FLUX® projects are created for each design step (each geometric parameter) and Python files utilised to change the parameter during the design as shown in Figure 3.5. A distinct modular approach to these files allows reuse of the Python file structure with only slight modifications required for the relevant geometric parameter being changed. An example Python file used during the electromagnetic design is given in Appendix A (for geometric parameter W_p).

The non-linear behaviour of the RSM requires a non-linear solver to solve the FEM problem. The non-linear solver used in FLUX® uses the well known Newton-Raphson Method [47]. Solving via the Newton-Raphson Method means that the system of equations defined by the FEM formulation is solved iteratively by performing a linearisation of the non-linear system at each iteration. This linearised system is then solved using an iterative linear solver. The linear solver used in FLUX® is the Generalised Minimum Residual Method (GMRES) as introduced by Saad and Schultz in [48] with an Incomplete LU factorisation with Threshold (ILUT) preconditioner as introduced by Saad in [49]. The various solving parameters are made

available to the user in FLUX® but can be left as an automatically selected default value. The user selected precision for the GMRES solver is 0.001 and the ILUT pre-conditioner has a tolerance of 0.001. The maximum number of iterations for the linear solver is dependant on the model (degrees of freedom) which has a strong link with the defined mesh. Once the linear system is solved at a particular iteration, the non-linear solver steps in again with a better estimation of the system unknowns. It then linearises the system around this new estimation and the linear solver will step in again and solve the new linearised system. This process continues until the non-linear solver converges and the solving will stop once the estimation of the system unknowns is determined to within a predefined user selected precision. It is important to define a finite number of iterations as the Newton-Raphson Method is an open method that can easily diverge and enter into an infinite loop and not actually solve the problem.

3.2.5 Magnetisation curve for electromagnetic FEM simulations

The inclusion of the magnetisation curve of the steel used for the stator and rotor allows for the designer to account for non-linear magnetic behaviour. The material entered in FLUX® is M400-50A steel. It is modelled by entering the discrete data pairs of magnetic flux density and magnetic field intensity (B_n, H_n) that define the materials' magnetic behaviour into a table. These data points are then used to do an isotropic spline fit. An example of this for M400-50A steel is shown in Figure 3.6 along with the original discrete data pairs entered in FLUX®.

3.2.6 Mesh for electromagnetic FEM simulations

The mesh used in the electromagnetic design has been chosen carefully so as to maximise accuracy in the most important areas of the geometry. An example of the mesh is shown in Figure 3.7. There are just under 2400 elements in this geometry with just over 52000 nodes. The most important sections in the geometry are the air-gap, the mechanical supports (radial ribs and tangential webs), the stator teeth and the rotor flux guides. The increased mesh density around the more important parts of the geometry is clearly seen in the zoomed views of the geometry in Figures 3.8(a) and 3.8(b).

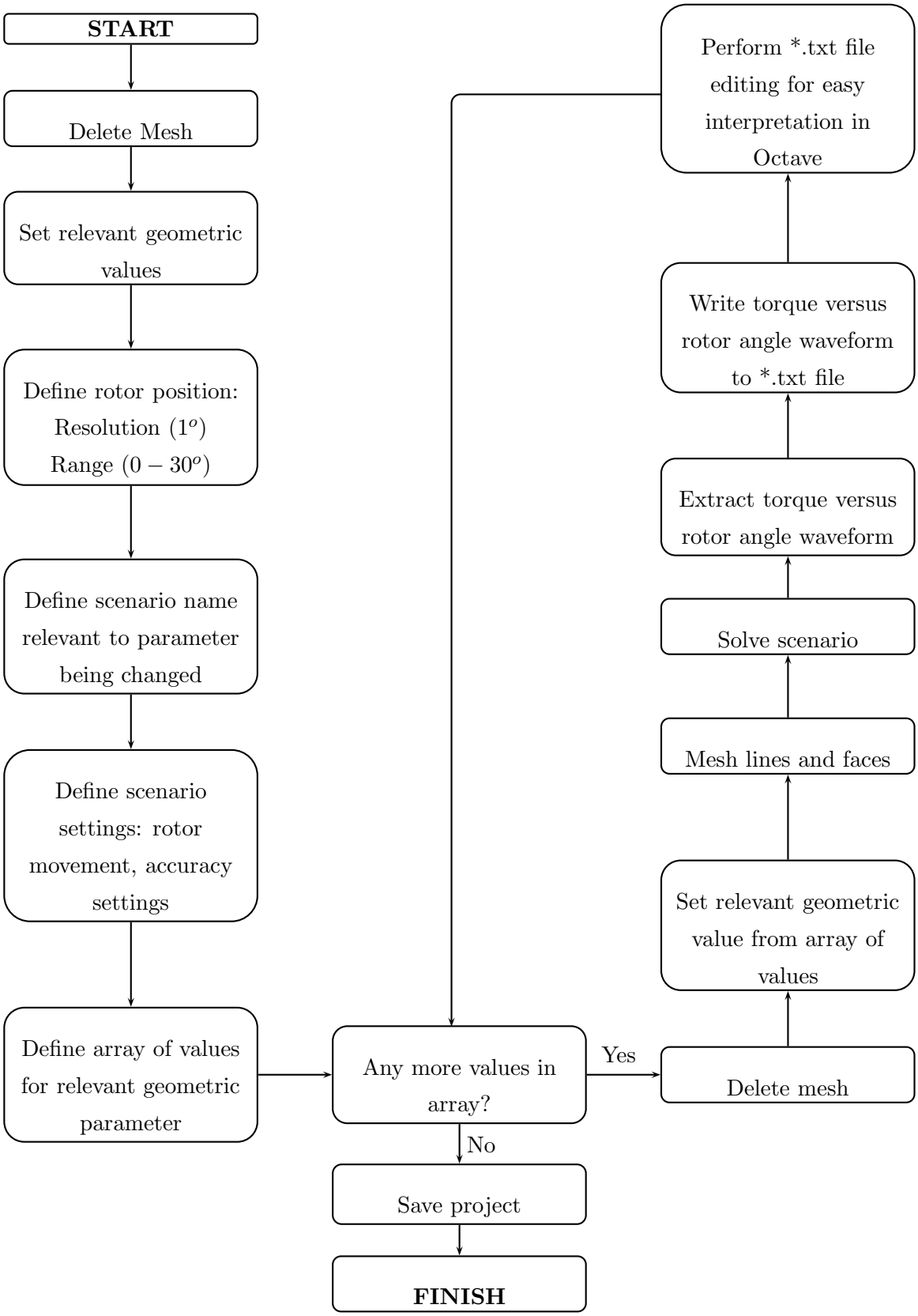


Figure 3.5: Modular structure of Python files used for electromagnetic design

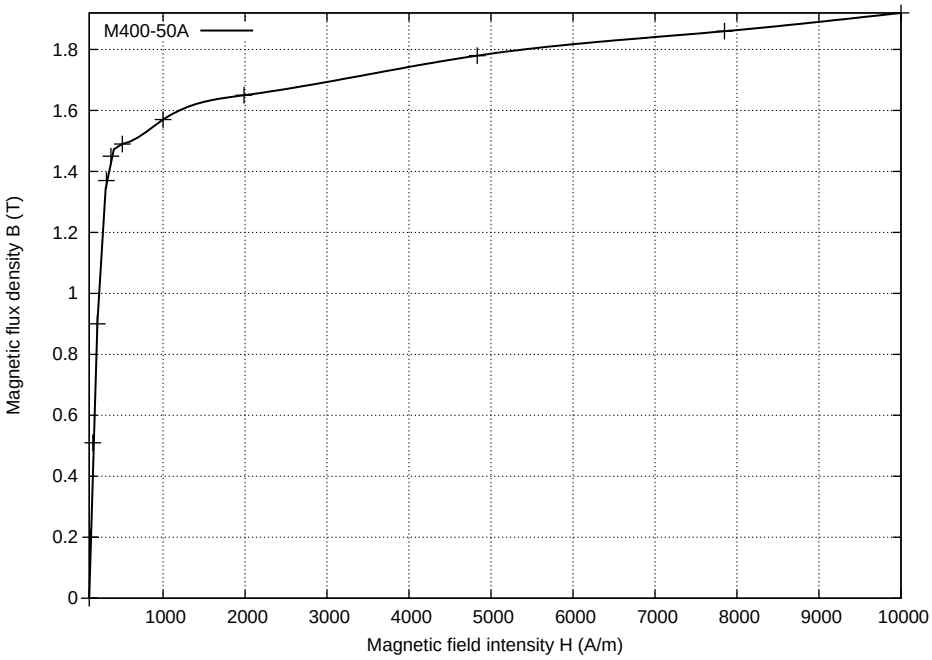


Figure 3.6: Magnetisation curve used for electromagnetic FEM

3.2.7 Electromagnetic FEM design results

The results from the electromagnetic design procedure are now presented. Analysis of the results reveals some interesting insight into the effects the five geometric parameters have on torque production.

Variation of N_{rb} and β

It has been shown by Matsuo and Lipo in [12] that a crucial parameter requiring significant attention in a RSM rotor design is the rotor insulation ratio:

$$\beta = \frac{b_{bw}}{b_{bw} + b_{lw}} \tag{3.20}$$

where

b_{bw} = Individual rotor barrier width

b_{lw} = Individual flux guide width

In this design procedure the number of rotor barriers investigated ranges from 1 to 30 along with an insulation ratio varying between 0.01 to 0.95. Mean torque and torque ripple versus insulation ratio plots for a range of rotor barriers are shown in Figure 3.9.

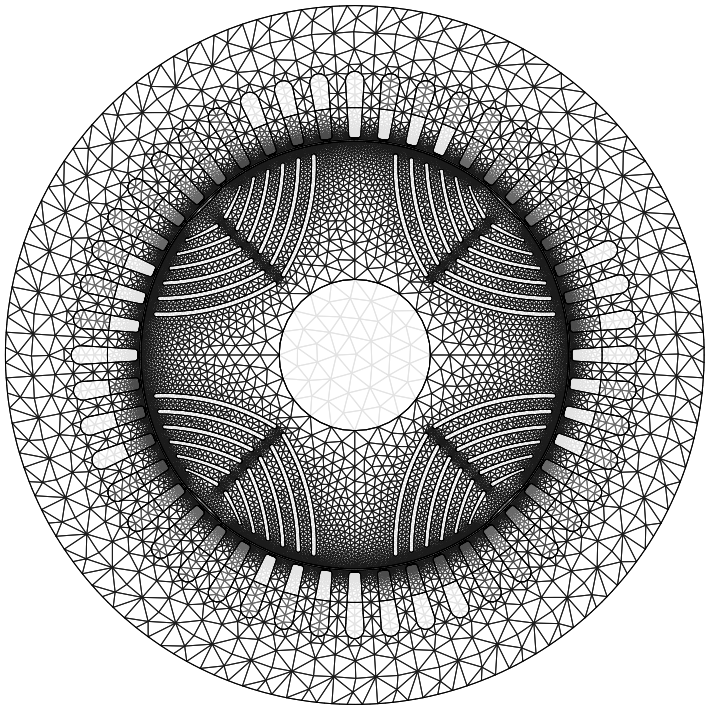
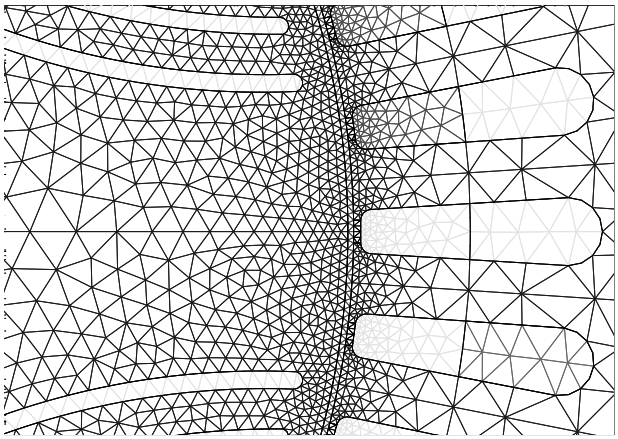


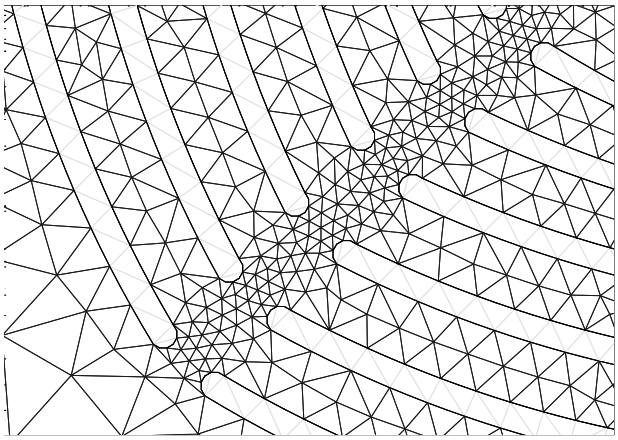
Figure 3.7: Example of the mesh used in electromagnetic simulations

It can be seen from Figure 3.9(a) that maximum mean torque occurs around $\beta = 0.3$ to $\beta = 0.4$ for rotor barrier numbers of five or more. The torque developed seems to *saturate* after barrier numbers higher than 10 are used. This seems to agree well with the findings in [13]. With more rotor barriers present, the rotor becomes mechanically weak without any added electromagnetic performance advantage. A higher number of rotor barriers will make manufacturing difficult and more costly as a result of the intricate rotor design. Therefore, a rotor barrier number around five or six seems feasible for this rotor size and would allow for high average torque (comparable to maximum average torque when N_{rb}=30) while still maintaining mechanical strength. An insulation ratio of $\beta = 0.3$ is chosen as a result of the average torque developed being at a maximum for a rotor barrier number of five and six. The final rotor barrier number is decided upon by looking at the torque ripple plots in Figure 3.9(b). The torque ripple for a rotor barrier number of five is around 30% whereas the torque ripple for a rotor barrier number of six is almost a third of that at around 10%. As a result, a rotor barrier number of six is chosen.

The values of insulation ratio that result in maximum average torque require a valid explanation. When the rotor insulation ratio is small it allows for more steel to be available for flux to travel in the D-axis and thus increases L_{dm} to result in an increase in torque [13]. However, there is a limit to the value of β where this stops



(a) Zoomed view of mesh on stator and rotor



(b) Zoomed view of radial ribs mesh

Figure 3.8: Zoomed views of electromagnetic mesh

happening as a result of the reduction in barrier thickness which causes L_{qm} to increase and thus torque would decrease. In [12], a value of $\beta = 0.33$ was chosen and in [46] the optimal value for $\beta = 0.4$ was chosen. In [6], the width of the flux barriers and flux guides are set equal to each other and thus a value of $\beta = 0.33$ is used. These results reinforce the choice of $\beta = 0.3$ in the current design.

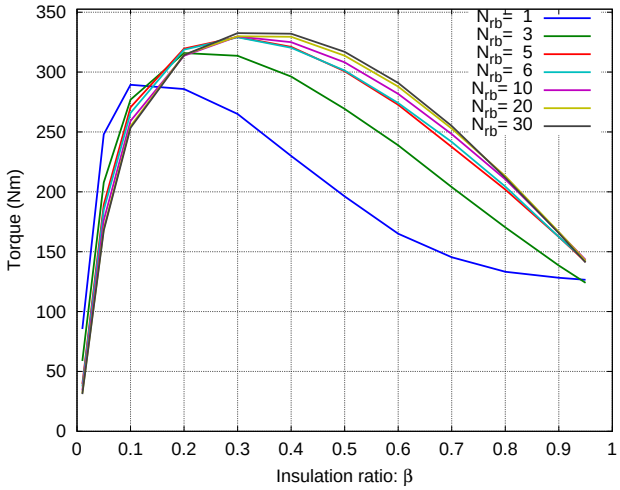
When choosing N_{rb} and β, Bomela and Kamper showed in [17] that by making the rotor barrier pitch (γ) wider than one stator slot pitch (κ), low-order harmonics of flux are attenuated and flux pulsations are avoided which would in turn reduce torque ripple. The rotor barrier pitch with $N_{rb} = 6$ and $W_p = 20$ mm is $\gamma = 4.6^o$. The stator slot pitch of the original stator is $\kappa = 7.5^o$. Thus, the chosen rotor barrier number of six results in a rotor barrier pitch that is not wider than one stator slot pitch. A rotor barrier number of five would result in a rotor barrier pitch of around $\gamma = 5.5^o$, a rotor barrier number of four would result in $\gamma = 6.8^o$ and

finally a rotor barrier number of three would result in $\gamma = 9.1^o$. Thus, only when the rotor barrier number is decreased to three will the rotor barrier pitch be larger than the stator slot pitch. However, as shown in Figure 3.9(a), with a rotor barrier number of three, the mean torque is considerably less than the mean torque with a rotor barrier number of six. More importantly, by considering Figure 3.9(b), torque ripple with a rotor barrier number of three is substantially higher than with the chosen rotor barrier number of six. Perhaps a better approach would be to redesign the stator so as to increase the number of stator slots and thus decrease the stator slot pitch. A brief discussion on this is given in the following paragraph and is discussed further in chapter 5.

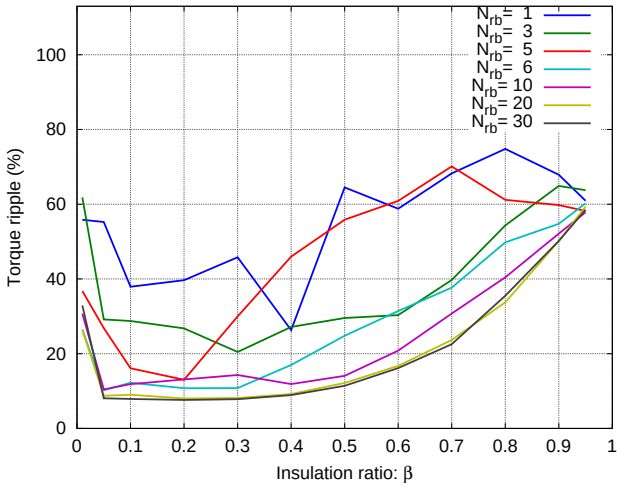
In the work by Vagati et al. in [20], an analytical approach to the minimisation of torque ripple is given. It is shown that with n_r separation points per pole pair on the RSM rotor and with n_s stator slots per pole pair, the choice of n_r should be $n_r = n_s \pm 4$ as a first step to minimising torque ripple. As an example, a 4-pole 48 slot stator should have a RSM rotor with $n_r = 20/28$. The worst case would be when $n_r = n_s$ ($n_r = 24$) [21]. For the chosen number of rotor barriers ($N_{rb} = 6$), $n_r = 30$ which is close to one of the suggested values of $n_r = 28$. If the analytical solution presented in [20] were to be used as the primary design choice - the stator could be redesigned to have $n_s = 26/34$ and therefore a 52 or 68 slot stator could be chosen. However, the work performed in [20] was only a first step to torque ripple minimisation and it is believed that the extensive FEM simulations performed constitute a more thorough approach.

Variation of W_p

With the number of rotor barriers set to six and $\beta = 0.3$, $\alpha = 1$ and $g = 0.8$ mm, the first barrier position W_p is changed in the range $W_p = 15$ mm to $W_p = 70$ mm. Torque and torque ripple versus rotor barrier position W_p are shown in Figures 3.10(a) and 3.10(b). As W_p increases there is an initial increase in mean torque but thereafter as the the rotor barriers move towards the Q-axis average torque decreases. A possible reason for this is as a result of less flux being linked with the high permeance D-axis as the rotor barriers move away from the D-axis and towards the Q-axis with the increase in W_p. This results in a decrease in D-axis inductance and an increase in Q-axis inductance which would decrease the torque index which directly affects torque development. Maximum mean torque occurs around $W_p = 20$ mm and minimum torque ripple at around $W_p = 25$ mm. A value of $W_p = 20$ mm is chosen as mean torque is considered a more important performance criteria as



(a) Mean torque



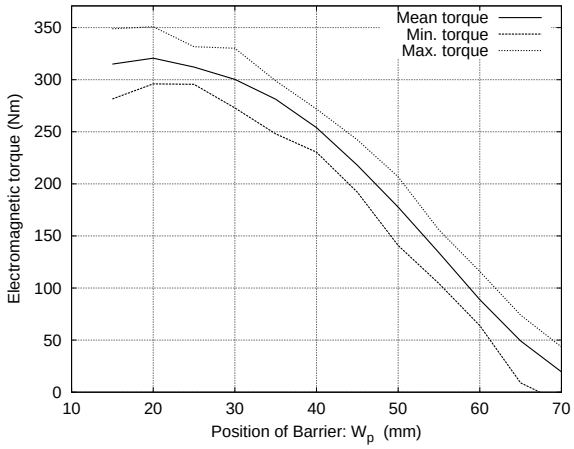
(b) Torque ripple

Figure 3.9: Mean torque and torque ripple versus beta for a range of rotor barriers

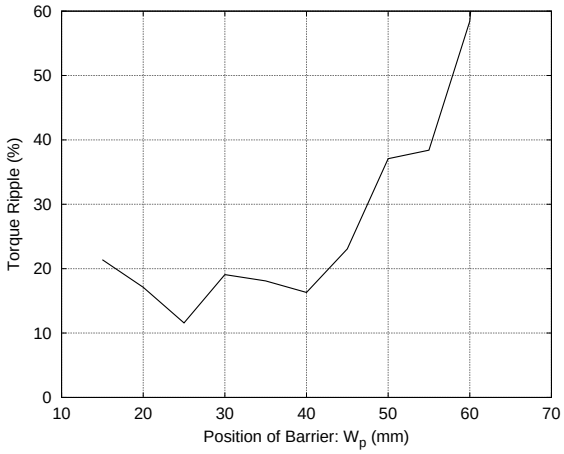
opposed to torque ripple. Torque ripple is a secondary performance criteria and can be reduced substantially using various design techniques, a few of which are introduced in chapter 5.

Variation of α

As can be seen in Figure 3.2, the parameter α is the geometric parameter that defines the amount of cut-out on the rotor. A rotor cut-out should significantly increase the



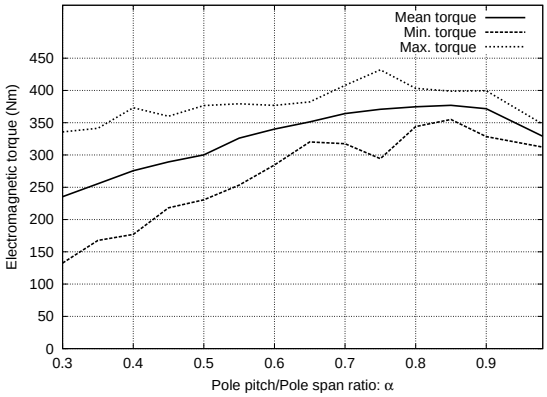
(a) Torque versus position of first rotor barrier



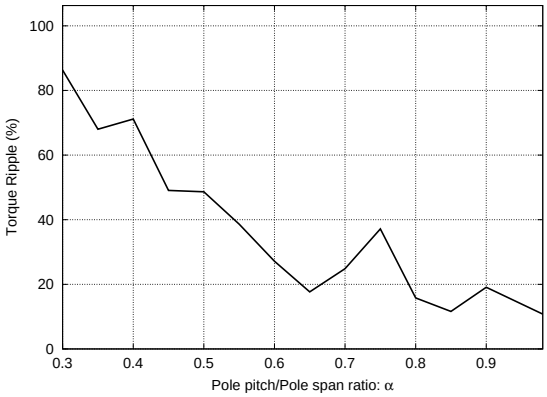
(b) Torque ripple versus position of first rotor barrier

Figure 3.10: Torque versus position of first rotor barrier W_p

reluctance in the Q-axis while leaving the D-axis reluctance relatively constant (up to a certain point). The parameter α is varied from 0.3 to 0.98. The reason for not decreasing α below 0.3 is that it cuts out so much of the rotor that the overall rotor structure becomes infeasible (the amount of cut-out goes beyond the radial width of the shaft). In Figures 3.11(a) and 3.11(b), torque and torque ripple versus pole pitch to pole span ratio plots are shown. As seen from these figures, maximum mean torque as well as minimum torque ripple occur around $\alpha = 0.85$. A value of $\alpha = 0.85$ is chosen for the rotor cut-out.



(a) Torque versus position of first rotor barrier



(b) Torque ripple versus position of first rotor barrier

Figure 3.11: Torque versus pole pitch to pole span ratio α

Variation of g

The nominal air-gap length of the original IM is 0.8 mm. The air-gap width for the new RSM is varied from g = 0.4 mm through to g = 1.2 mm. The torque versus air-gap length is shown in Figure 3.12. As expected, mean torque increases significantly as the air-gap length decreases. This is as a direct result of the D-axis inductance increasing as it is inversely proportional to air-gap width. The Q-axis inductance does not increase significantly with the decrease in air-gap width as it already has a very large effective air-gap on the Q-axis as a result of the numerous rotor barriers. Torque ripple increases as the air-gap length decreases as a result of the increased interaction between the stator slots and rotor barriers as they approach one another. Before opting for a smaller air-gap, consideration should be given to whether a significantly smaller air-gap is obtainable considering manufacturing tolerances. After consultation with the original IM manufacturer, a conservative design choice is made to leave the air-gap at the nominal value of $g = 0.8$ mm.

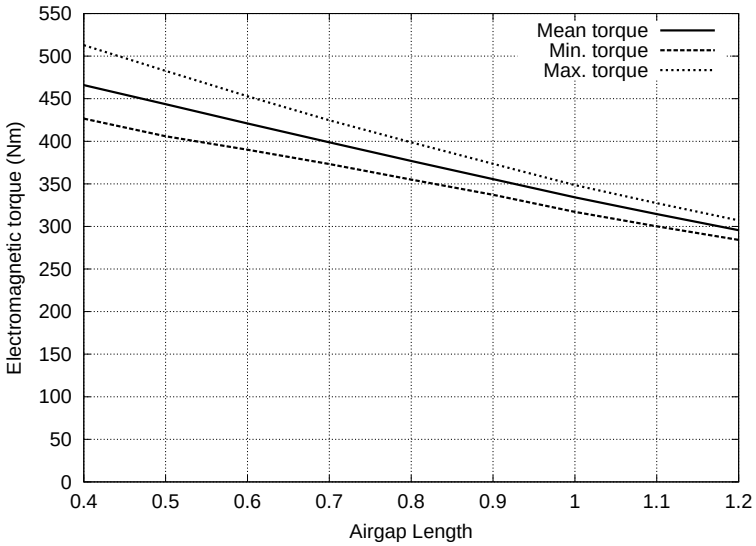


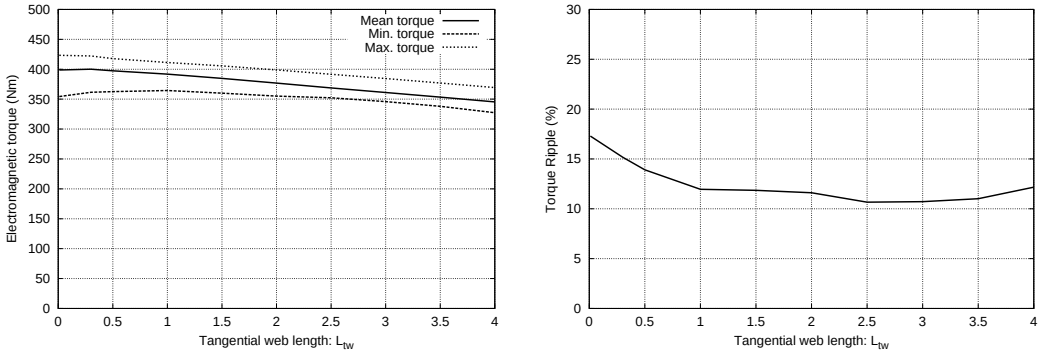
Figure 3.12: Torque versus air-gap length

Variation of l_{tw} and l_{rr}

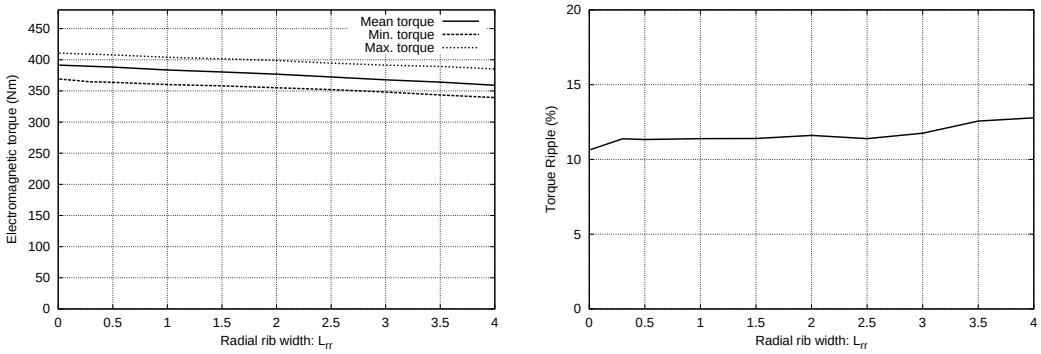
Purely for investigative purposes, the mechanical support parameters l_{tw} and l_{rr} are varied. The parameters are varied between 0.01 mm (almost zero) and 4 mm. Torque versus l_{tw} and l_{rr} plots are shown in Figures 3.13(a) and 3.13(b). As expected, mean torque decreases as l_{tw} and l_{rr} increase. An interesting result is how torque ripple increases when l_{tw} is close to zero as a result of an increased magnetic reaction between the stator slots and rotor barriers. This is similar to what occurs in the ALA rotor where the rotor barriers are directly on the rotor surface. The torque ripple that results has often been cited as a problem in the ALA rotor [21]. The same effect is not noticed when l_{rr} is close to zero as these supports do not lie on the rotor surface and thus do not affect torque ripple in the same way. Traditionally, as a rule of thumb, a few RSM designers have chosen the length of l_{tw} and l_{rr} to be a multiple of the lamination thickness [6, 30]. Initial electromagnetic design choices of $l_{tw} = 2$ mm and $l_{rr} = 2$ mm (four times lamination thickness) are chosen.

3.2.8 Final electromagnetic design

The final choices for the geometric parameters after the electromagnetic design are shown in Table 3.2. One pole of the final electromagnetic design is shown in Figure 3.14. The final electromagnetic design develops an average torque of 377 Nm with a torque ripple of 11.6%.



(a) Torque and torque ripple versus length of tangential web



(b) Torque and torque ripple versus length of radial rib

Figure 3.13: Torque versus lengths of rotor supports

Table 3.2: Final values of geometric parameters after electromagnetic design

Parameter	**Value**
N_{rb}	6
β	0.3
W_p (mm)	20
α	0.85
g	0.8
l_{tw} (mm)	2
l_{rr} (mm)	2

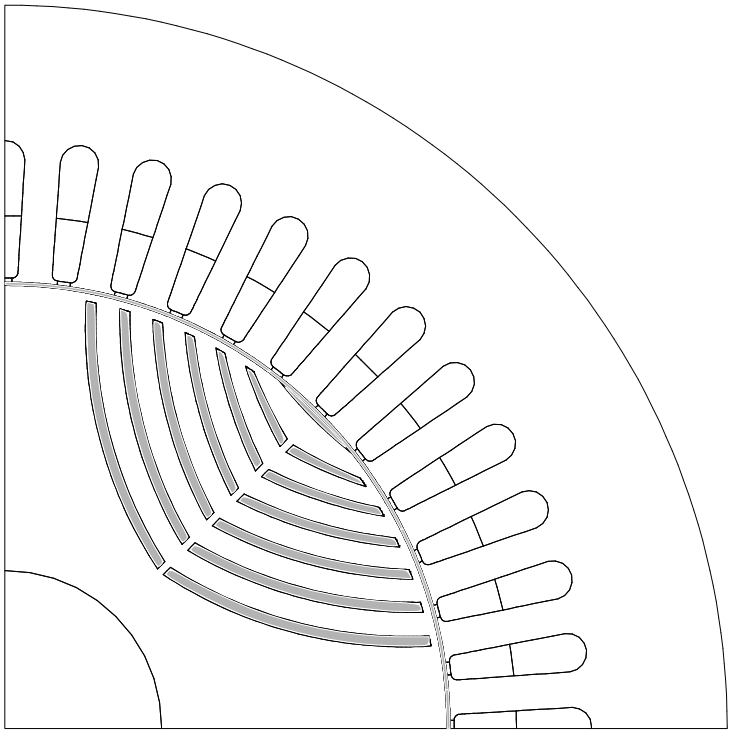


Figure 3.14: Cross section of RSM rotor after electromagnetic design

3.3 Mechanical FEM case studies

In [23], analytical equations modelling the stresses present in a modified IM rotor were presented. The equations present a very rough estimate of the stresses that would be present in the rotor structure. The usefulness of these calculations are limited and not sufficient to determine the localised stresses present in very important parts of the RSM rotor like in the tangential webs and radial ribs. Thus, mechanical FEM is carried out with the designed RSM rotor presented in Figure 3.14 as a starting point to verify mechanical strength when rotating at rated or above rated speed and when undergoing transient torque changes. An example of this is presented by Sibande et al. in [14] where mechanical FEM was performed to verify the strength of a newly designed RSM rotor with added Permanent Magnets (PMs).

There is a clear offset between electromagnetic and mechanical requirements with regards to the mechanical support parameters l_{tw} and l_{rr}. Electromagnetically speaking, they should be zero to maximise saliency but for mechanical support, they need to be non-zero. To investigate the necessary widths of l_{tw} and l_{rr} that result in a mechanically strong rotor, 2-Dmechanical FEM analysis in ANSYS® is performed.

3.3.1 Types of mechanical analyses

The scalar von Mises stress plot is used to analyse the mechanical strength of the RSM rotor. It is traditionally used to predict yielding of structures and is thus quite applicable for this analysis. The mechanical properties of the material used (M400-50A steel) are a Poissons ratio of $\nu = 0.29$ and a Youngs modulus of $E_y = 200$ GPa. The mechanical analysis is based on three case studies:

- Case I: Analysis of the original electromagnetic designed RSM rotor.
- Case II: Case I with rounded barrier edges.
- Case III: Case II with wider mechanical supports.

3.3.2 Types of loads

The mechanical loads chosen for the rotor are mechanical angular velocity and angular acceleration inertia loads. The mechanical angular velocities simulated are twice rated speed $\omega_m = 100\pi$ rad/s (3000 rpm) and rated speed $\omega_m = 50\pi$ rad/s (1500 rpm). The angular acceleration load is chosen so as to simulate a mechanical torque requirement on the rotor. It is based on a simplification of equation 2.10 where the equivalent friction coefficient is ignored and mechanical speeds are considered:

$$T_{el} - T_{mech} = J_{eq}\frac{d\omega_m}{dt} \tag{3.21}$$

where

ω_m = Mechanical angular velocity

The mechanical angular velocity is related to the electrical angular velocity by the well known relation $\omega_m = \dfrac{\omega}{P}$. Using equation 3.21, a reasonable case to consider would be when the RSM is developing no electromagnetic torque ($T_{el} = 0$ Nm) and the mechanical torque requirement is twice the rated torque. Thus, if an approximation of the rated output torque of the RSM is used (≈ 400 N.m), the mechanical torque requirement would be $T_{mech} = 800$ Nm. Thus, the left hand side of equation 3.21 is simply 800 Nm. An approximation of the moment of inertia is chosen based on a cylindrical billet of steel ($J_{eq} \approx 0.4$ kg.m^2). From these values, the angular acceleration load is approximated as 2000 rad/s^2.

3.3.3 Mechanical FEM design results

The highest mechanical stresses in the rotor occur on the innermost radial rib. This is as a result of the innermost radial rib being required to hold in the largest mass of the rotor. In the next sections the results from the three case studies will focus on this innermost radial rib.

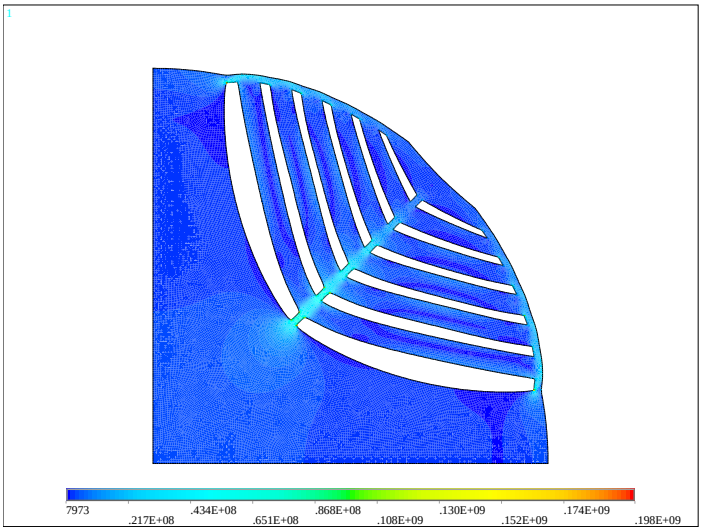
Case I

The von Mises stress contour plot of the RSM rotor with straight edges at twice rated speed (3000 rpm) is shown in Figure 3.15(a). The exaggerated displacement of the RSM rotor can be clearly seen in Figure 3.15(a). A zoomed view of the innermost radial rib is shown in Figure 3.15(b). As expected, the stresses in the rotor are pronounced around the straight edges of the rotor barriers with the highest stress of 198 MPa being on the innermost rotor barrier. Clearly, the straight edged rotor barriers are a problem mechanically and the general shape of the rotor barrier edges should be changed.

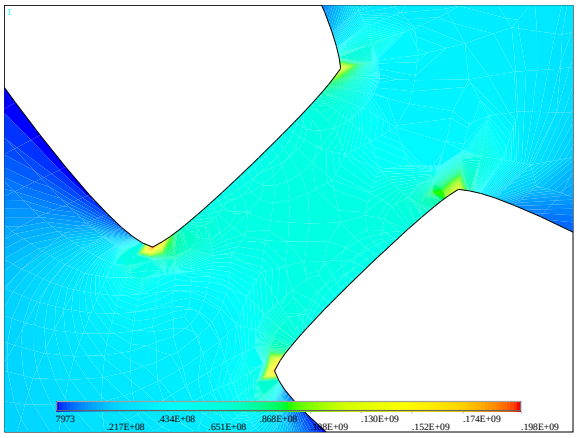
Another important mechanical aspect to consider is the physical distortion of the rotor. The contour plot of the physical distortion of the RSM rotor shown in Figure 3.16 shows that the maximum mechanical distortion of the rotor is 8.6 μm and occurs in the rotor barriers. The slight asymmetrical nature of the rotor distortion is as a result of the angular acceleration load imposed on the rotor concurrently with the angular velocity load. The angular acceleration load is imposed so as to attempt to accelerate the rotor in the anti-clockwise direction.

Case II

The original electromagnetic RSM rotor geometry is adjusted so that the rotor has rounded barrier edges. It is expected that the maximum stress in the rotor should decrease substantially. The stress contour plot for the new rounded barrier edge rotor is shown in Figure 3.17(a). A zoomed view of the innermost radial rib is shown in Figure 3.17(b). As expected, the maximum stress on the innermost barrier has reduced substantially to 95 MPa. This is less than half the maximum stress present in Case I. This is a very promising result since the rotor has become significantly stronger after merely changing the shape of the rotor barrier edges and not actually widening the mechanical supports.



(a) von Mises stress contour plot for Case I



(b) Zoomed view of von Mises stress contour plot for Case I

Figure 3.15: von Mises stress plots for Case I

A contour plot of the displacement of the rotor is shown in Figure 3.18. The maximum mechanical distortion of the rotor is 8 μm and occurs around the same location as in Case I (in the rotor barriers). Only a slight reduction in displacement is noticed between Case I and II. This is more than likely due to the mechanical support widths not being increased. It is only the shape of the rotor barrier edges that have been changed.

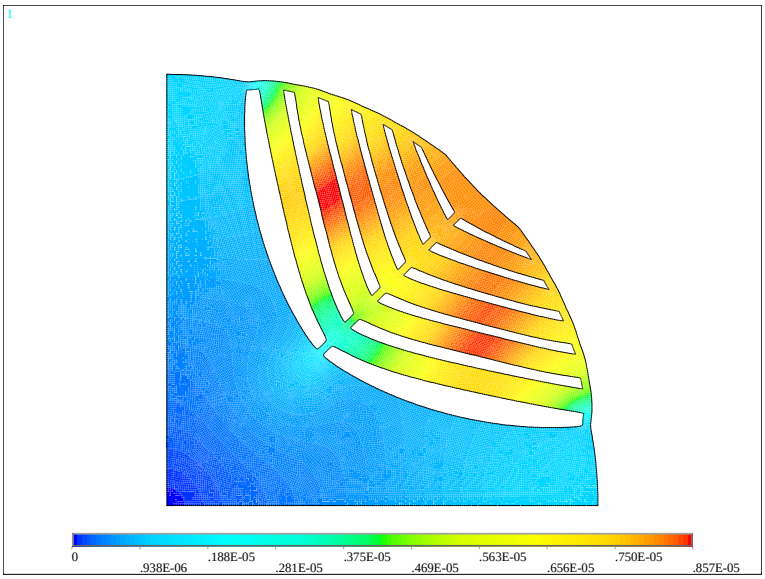


Figure 3.16: Displacement contour plot for Case I

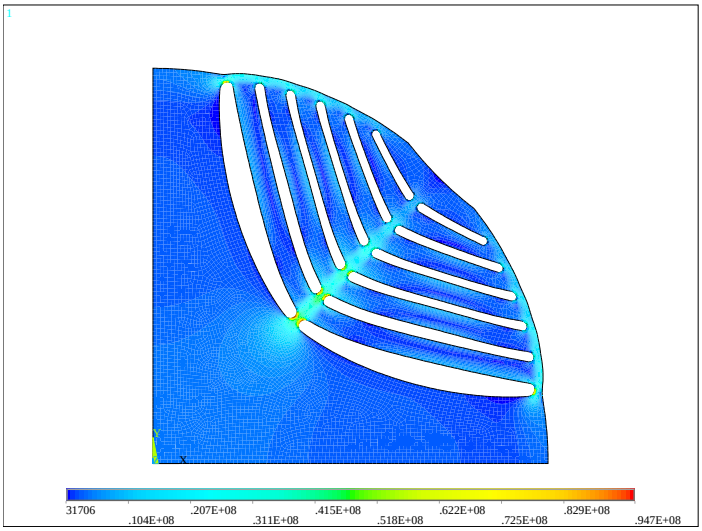
Case III

The geometry in this analysis is based on the geometry in Case II but with wider tangential webs and radial ribs. The lengths of l_{tw} and l_{rr} have been doubled to 4 mm. The stress contour plot is shown in Figure 3.19(a) with a zoomed view of the innermost radial rib shown in Figure 3.19(b). The stresses have reduced significantly to around 60 MPa. It is interesting to note how the stress distribution between the rotor barriers has decreased significantly. This is very important as these areas will be stressed the most during operation and will fatigue over time.

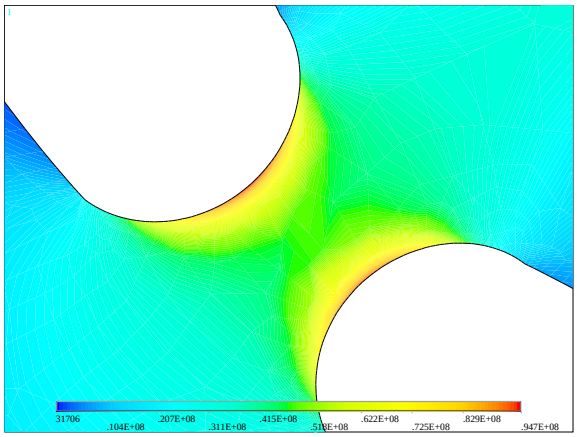
With the wider mechanical supports, the displacement contour as seen in Figure 3.20 reveals a maximum displacement of the rotor of 5.8 μm. This is considerably lower than Cases I and II and reveals the increase in mechanical rigidity of the rotor as a result of the wider mechanical supports.

Discussion of mechanical FEM results

The material used in the RSM rotor (M400-50A steel) has a yield strength of 320 MPa. If a safety factor of ten is chosen (harsh mining environment) then the maximum stress that should be present in the rotor should be 32 MPa. Based on the operating stresses revealed in Cases I - III, Table 3.3 is drawn up. As can be seen in Table 3.3,



(a) von Mises stress contour plot for Case II



(b) Zoomed view of von Mises stress contour plot for Case II

Figure 3.17: von Mises stress plots for Case II

a safety factor of 5.39 is the highest safety factor attained when at twice rated speed. This may seem disheartening but an angular velocity inertia load of twice the rated speed has been imposed. This case will not always occur and it is more likely that this is a special case and on average the machine will operate closer to rated speed. Simulations of Cases I-III with a more likely angular velocity of rated speed $\omega_m = 50\pi$ rad/s (1500 rpm) have been performed with interesting results as shown in Table 3.3. As can be seen, the mechanical safety factor is larger than ten for Cases II and III. After consultation with the motor manufacturer, a conservative RSM rotor construction with rounded barrier edges and mechanical supports $l_{tw} = 4$ mm and $l_{rr} = 4$ mm is chosen (Case III).

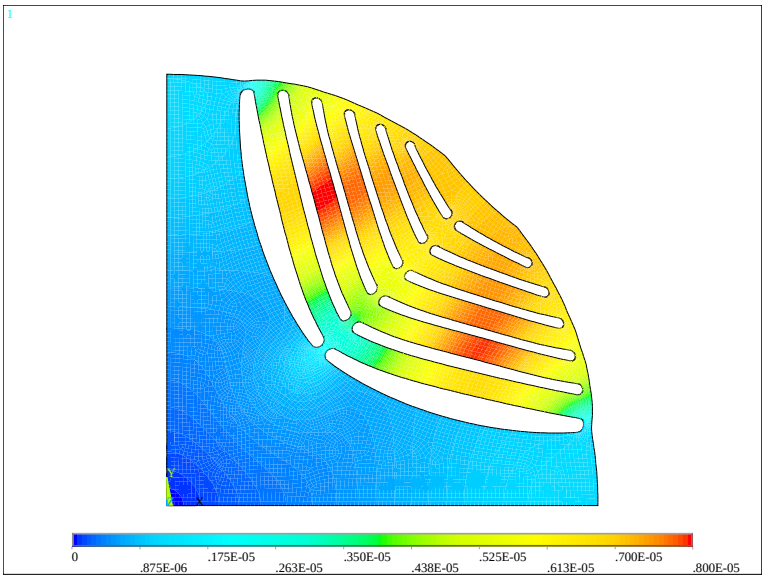


Figure 3.18: Displacement contour plot for Case II

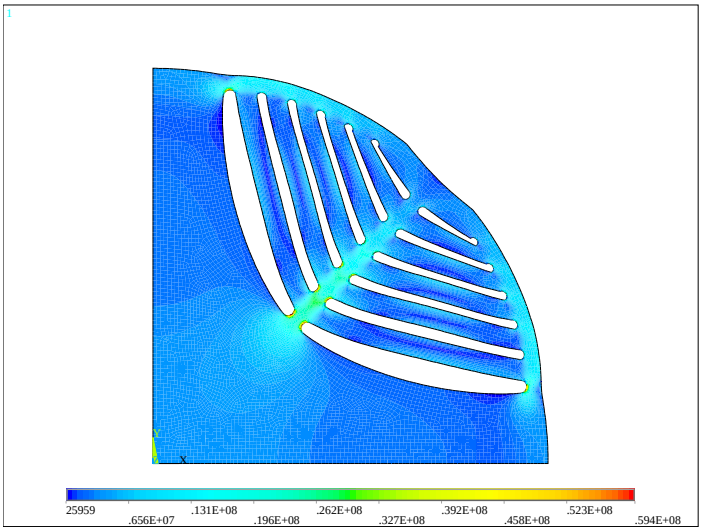
A cross section of the final RSM rotor design with the required manufacturing geometric artefacts (key-way and axial bars) is shown in Figure 3.21. The full geometric details of the final RSM are revealed in Appendix B.

3.4 Inductances of the final RSM design

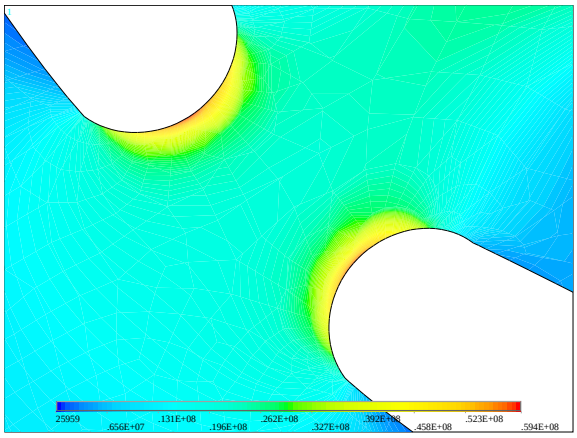
The inductances L_{dm} and L_{qm} of the final RSM can be determined directly from FEM calculations by analysing the fundamental component of the air-gap flux density waveform with the relevant D or Q-axis current excitation [12, 41]. Equiflux plots of when D and Q-axis excitation is present are shown in Figures 3.22(a) and 3.22(b) respectively. The inductances can be determined by using the following equations:

$$L_{dm} = (\frac{K_w N_1}{N_c}) \frac{D l_{Fe} B_{1d}}{P i_{ds}} \tag{3.22}$$

$$L_{qm} = (\frac{K_w N_1}{N_c}) \frac{D l_{Fe} B_{1q}}{P i_{qs}} \tag{3.23}$$



(a) von Mises stress contour plot for Case III



(b) Zoomed view of von Mises stress contour plot for Case III

Figure 3.19: von Mises stress plots for Case III

where

K_w = Fundamental winding factor
N_1 = Number of turns per phase
N_c = Number of parallel circuits per phase
D = Stator bore diameter
l_{Fe} = Effective stack length
B_{1d} = Fundamental component of D-axis air-gap flux density waveform
B_{1q} = Fundamental component of Q-axis air-gap flux density waveform

Examples of the D and Q-axis air-gap flux density waveforms over one pole pair are shown in Figures 3.23(a) and 3.23(b). Superimposed on top of the air-gap flux

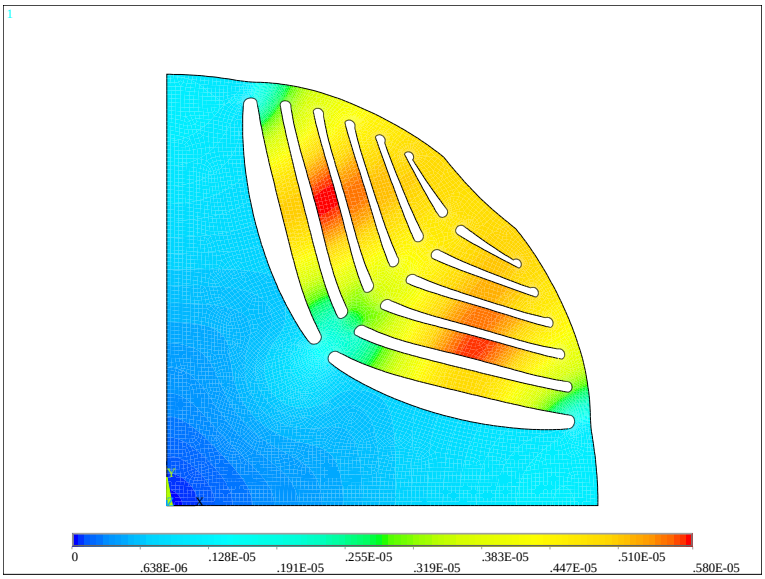


Figure 3.20: Displacement contour plot for Case III

Table 3.3: Stresses and safety factors for three mechanical FEM investigations

$\omega = 100\pi$ rad/s $\alpha = 2000$ rad/s^2	**Goal value**	**Case I**	**Case II**	**Case III**
s_{yield} (MPa)	320	320	320	320
s_{op} (MPa)	32	198	94.7	59.4
n_{op}	10	1.62	3.38	5.39
$\omega = 50\pi$ rad/s $\alpha = 2000$ rad/s^2				
s_{yield} (MPa)	320	320	320	320
s_{op} (MPa)	32	54.7	24.8	16
n_{op}	10	5.85	12.9	20

density waveforms are the fundamental components of the D and Q-axis waveforms. The D and Q-axis magnetising inductances (L_{dm} and L_{qm}) are determined for a range of D and Q-axis current excitations ranging from 10 A to 150 A rms so that the inductance variation as a result of saturation can be revealed. The inductances are plotted as a function of the relevant D and Q-axis excitation in Figure 3.24. As can be seen, the magnetic steel saturation results in a decrease in inductance on both axes as current excitation increases with this effect being exaggerated on the D-axis. The torque index ζ of the final RSM design, calculated using equation 2.13,

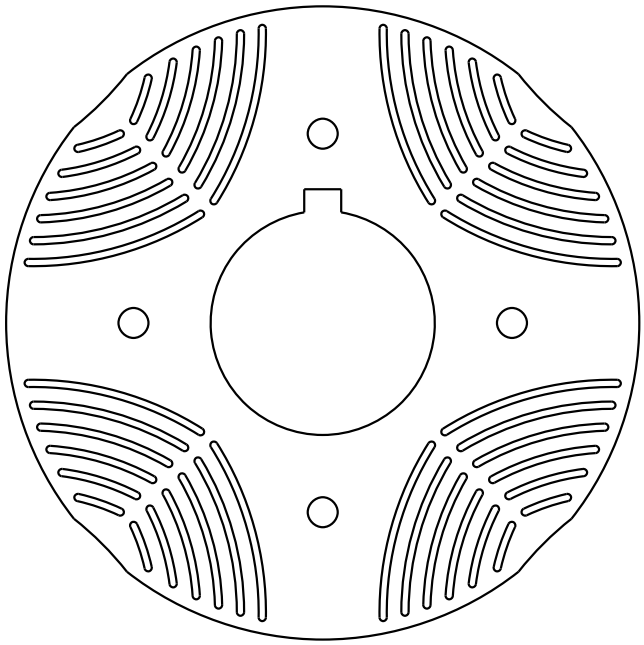


Figure 3.21: RSM cross section after electromagnetic and mechanical design

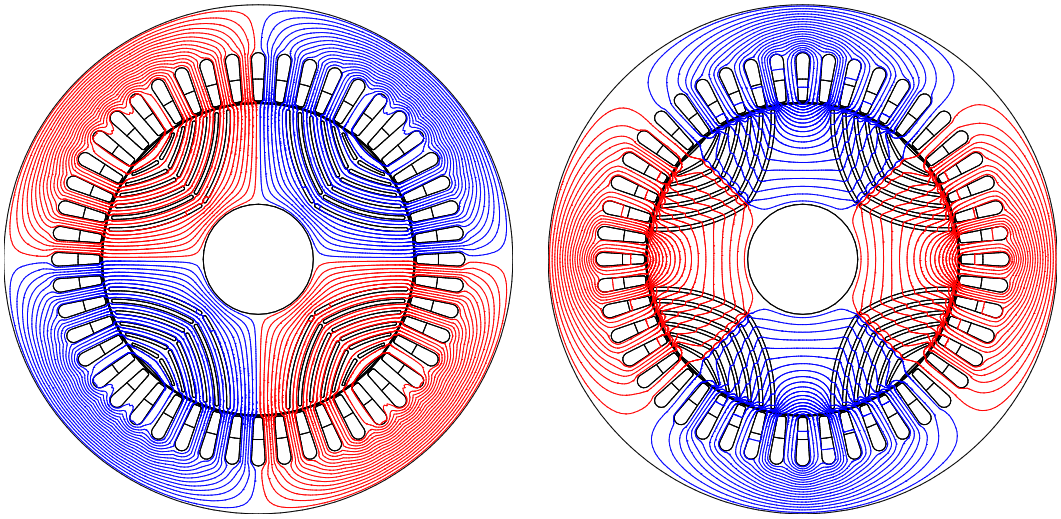
as a function of current excitation is shown in Figure 3.25.

3.5 Electromagnetic performance of RSM case studies

Brief electromagnetic FEM studies are presented analysing the electromagnetic performance of the mechanical case studies presented in section 3.3. The first electromagnetic study will compare the torque performance of Case I (the electromagnetic RSM design) with Case II to investigate the effect of rotor barrier shape on electromagnetic performance. The second study compares Case II and Case III to investigate the electromagnetic effect of the mechanical support widths being widened.

3.5.1 Comparison of Case I with Case II

As can be seen from Figure 3.26, where torque developed by Case I and Case II are compared, the torque performance remains relatively the same. The mean torque changes from 377 Nm in Case I to 373 Nm in Case II, a change of only 1%. The torque ripple changes from 11.6% in Case I to 9.9% in Case II which shows a slight reduction in torque ripple. This could be as a result of the smoother barrier edges in



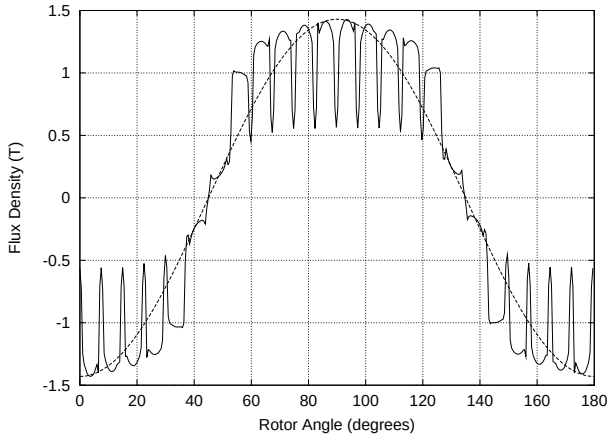
(a) Purely D-axis excitation (b) Purely Q-axis excitation

Figure 3.22: Equiflux plots with D and Q axis excitation

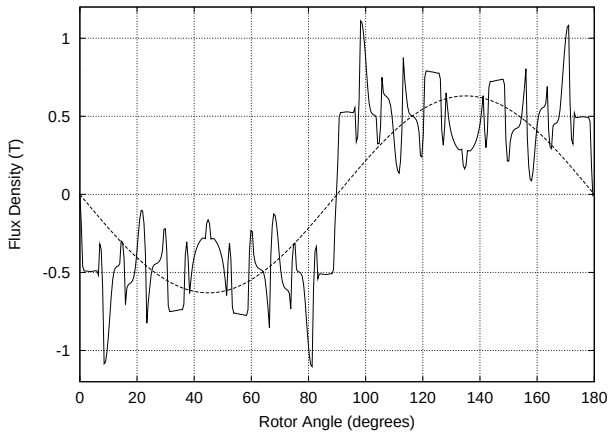
Case II allowing flux to flow more easily from the stator to the rotor. This effect can be seen graphically by the equiflux plots shown in Figure 3.27 where the rounded barrier edges (Figure 3.27(b)) allow for the flux to flow past them much easier than the straight barrier edges (Figure 3.27(a)).

3.5.2 Comparison of Case II with Case III

Case III has mechanical supports l_{tw} and l_{rr} set to 4 mm which is double the widths of the mechanical supports in Case II. The electromagnetic performance of Case III is expected to degrade as a result of a lower reluctance path now available on the Q-axis as a result of the wider mechanical support widths. The expected performance degradation is verified in Figure 3.28. A 16% reduction in mean torque from 377 Nm in Case II to 325 Nm in Case III is noted. The offset between electromagnetic design requirements (maximum mean torque) and mechanical requirements (safety factor) is clearly seen here. Although better electromagnetic performance may have been attained with smaller mechanical supports (Case II), the rotor would not be strong enough mechanically to withstand the stresses it would experience. As a result, wider mechanical supports are chosen in the final RSM design (Case III).



(a) D-axis air-gap flux density waveform with $i_{ds} = 93$ A, $i_{qs} = 0$ A



(b) Q-axis air-gap flux density waveform with $i_{qs} = 93$ A, $i_{ds} = 0$ A

Figure 3.23: Flux density waveforms with D and Q-axis excitation

3.6 Summary

A brief Finite Element Method (FEM) background has been given revealing the basic idea of how FEM approaches a large spatial problem by breaking it down into finite elements and then solving a set of matrix equations (possibly non-linear) using numerical methods. A 2-D magnetostatic application is used for the design of the RSM and thus background knowledge on magnetostatic FEM is given.

The electromagnetic design is performed using FLUX®. The design investigates the effects that five geometric parameters have on torque production. This design procedure calculates torque at each rotor position over a predefined rotor angle with the relevant stator current excitation. The average torque and torque ripple

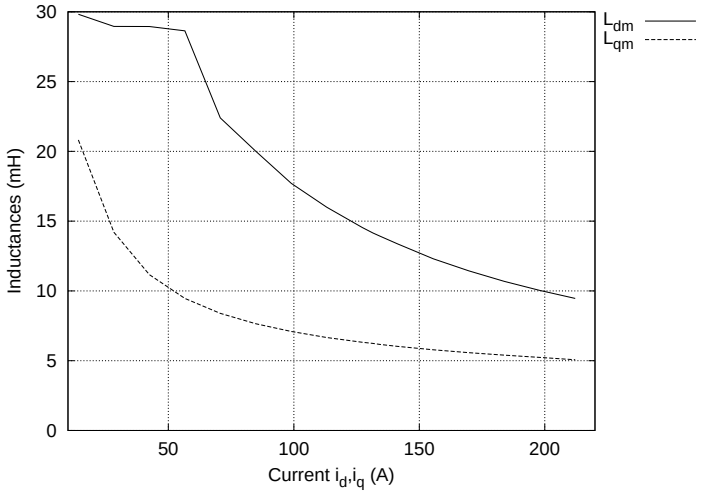


Figure 3.24: D and Q axis magnetising inductances for a range of currents

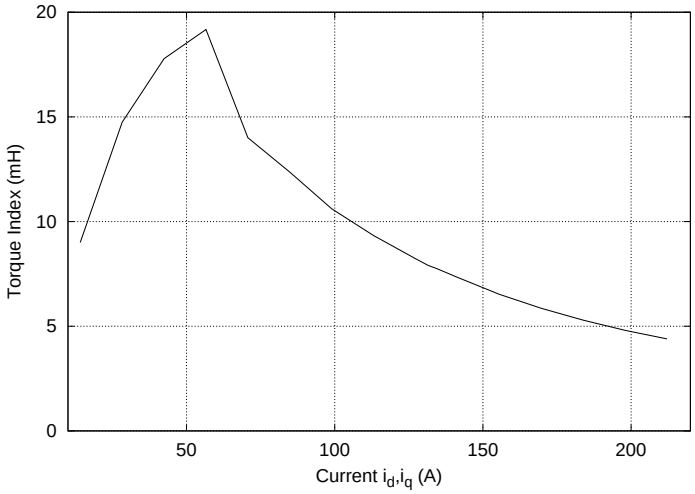


Figure 3.25: Torque index of final RSM rotor

are extracted from the resultant torque waveform. The five geometric parameters varied are number of rotor barriers N_{rb}, rotor insulation ratio β, the position of the first rotor barrier from the D-axis W_p, rotor pole pitch to pole span ratio α and air-gap length g. The geometric parameters are varied in a linear progression (one at a time). The choices for the final values of the geometric parameters are made by choosing where maximum mean torque and minimum torque ripple occurs. A rotor barrier number of six is chosen along with a rotor insulation ratio of $\beta = 0.3$. The rotor cut-out value of $\alpha = 0.85$ allowed for good torque production and low torque ripple. Even though significantly more torque would be produced if a smaller air-gap was chosen, the air-gap length was left at the nominal value of 0.8 mm.

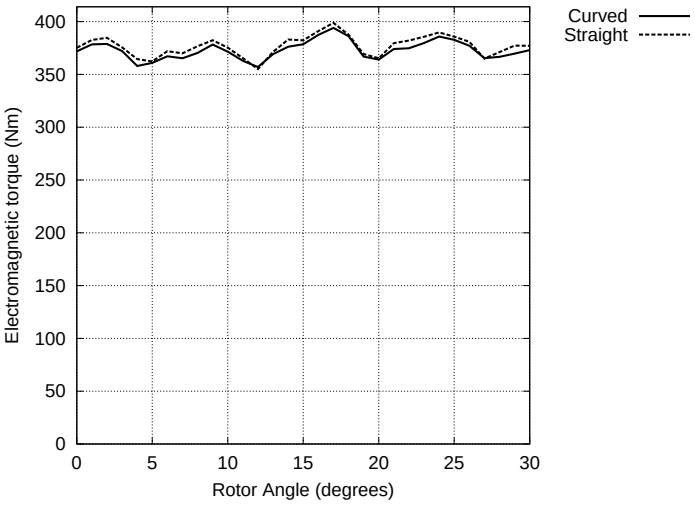
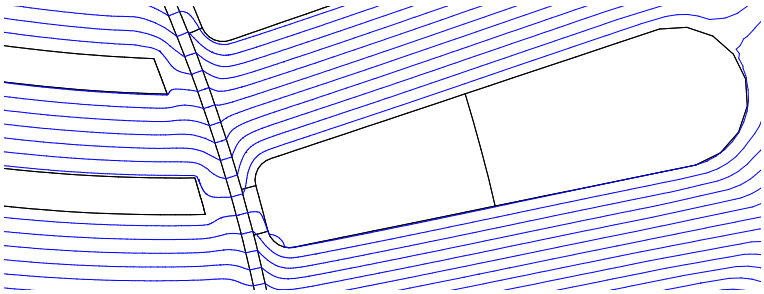
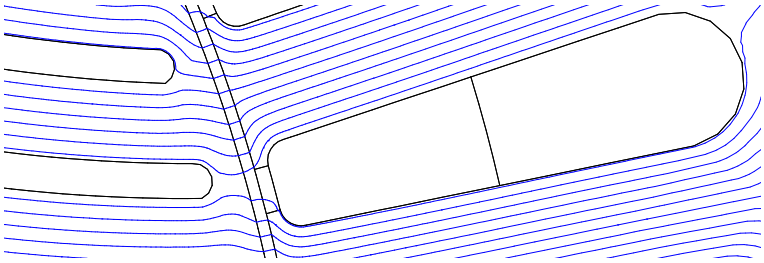


Figure 3.26: Comparison of torque with straight and rounded barrier edges

The two mechanical support geometric parameters l_{tw} and l_{rr} are determined in a mechanical FEM investigation in ANSYS®. The mechanical FEM investigation is based on the maximum von Mises stress present in the rotor at rated speed and twice rated speed with an additional angular acceleration load imposed. Three case studies were investigated. It was found that safety factors of ten or more were attained with rounded barrier edges and wider mechanical support widths of 4 mm when at rated speed. A conservative choice of mechanical support widths of 4 mm was made for the final RSM rotor. The obvious trade-off between electromagnetic performance and mechanical stability is clearly revealed in the electromagnetic FEM analysis of the three geometries outlined in the mechanical case studies. Wider mechanical support widths result in a more mechanically stable RSM rotor but result in reduced average torque ability.



(a) Zoomed view of equiflux plot for Case I



(b) Zoomed view of equiflux plot for Case II

Figure 3.27: Equiflux plots for Cases I and II

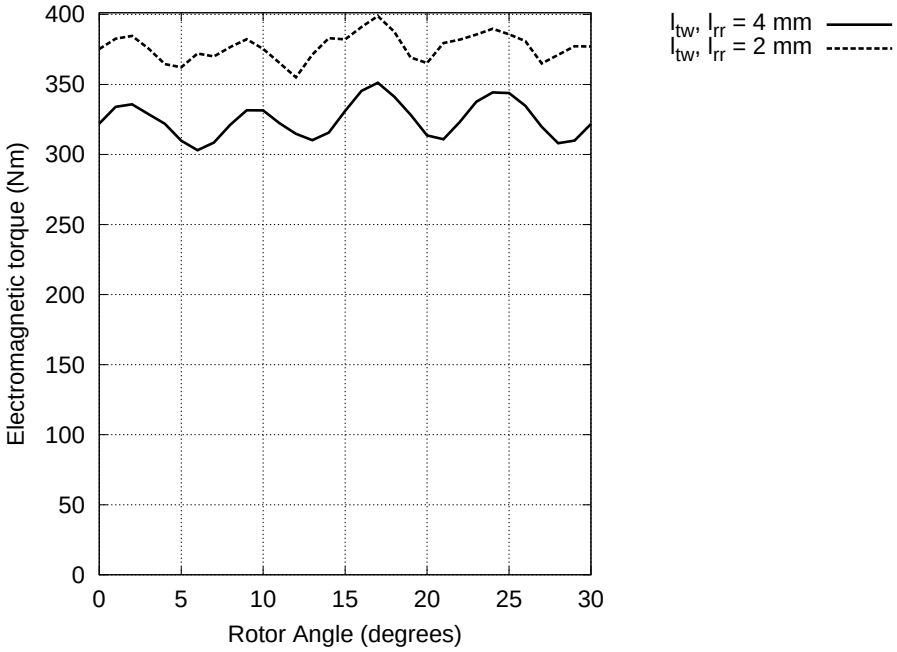


Figure 3.28: Comparison of torque with different mechanical support widths

Chapter 4

Comparison of RSM and IM Simulation Results

A comparison between FEM simulation results for the final RSM design and the previous solution (the IM) is presented in this chapter. The prioritised performance criteria, torque, is the focus of the simulation results presented.

4.1 RSM and IM cross sections

The technical details of the original IM are given in Appendix C. A cross section of the modelled original IM is shown in Figure 4.1. The final RSM design after the electromagnetic design and mechanical case studies is presented again in Figure 4.2 for convenience.

4.2 RSM and IM comparison

In [50], a range of simulations were performed on the IM in FLUX® with laboratory tests to backup simulation results. The calculated torque from FEM simulations for the IM with $I_{rated} = 93$ A is around 355 Nm. When operating at the same current level, the RSM develops an average torque of 325 Nm (8.4% less than the IM). It should be noted that if the IM is run from a modern VSD (as is the case for the underground shuttle vehicle), it needs to be derated. The designed RSM does not need to be derated in the same way as the IM as it does not contain a rotor cage. As a result, it could in fact develop more torque than the IM if this derating was

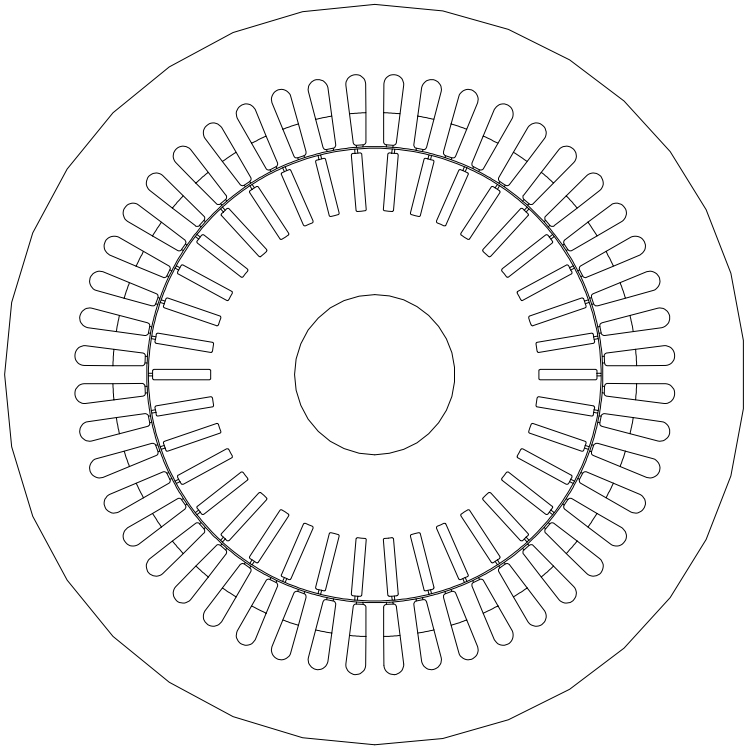


Figure 4.1: Cross section of original IM

taken into account. Also, the primary reason for the torque generated by the RSM being lower than the IM is as a result of the increased width of the mechanical supports l_{tw} and l_{rr} to 4 mm in the final design. With the mechanical supports set at 2 mm (mechanical case studies I and II), the torque generated is 377 Nm and 373 Nm respectively (6.2% and 5% higher than the IM respectively). The offset between electromagnetic performance and mechanical strength is clearly seen here.

4.3 RSM and IM comparison with RSM operating at MTC

The torque developed by the RSM with a current angle of $\theta_i = 60^o$ may not result in accurate MTC. This can be better understood by considering a normalised torque versus current angle curve for the designed RSM as shown in Figure 4.3. As can be seen, around 96% of maximum mean torque is developed at a current angle of 60^o. Maximum mean torque actually occurs around a slightly smaller current angle of 53^o. Thus, if a current angle around 53^o was chosen, the RSM in Case III would be able to generate up to 340 Nm of torque. This essentially halves the percentage by which

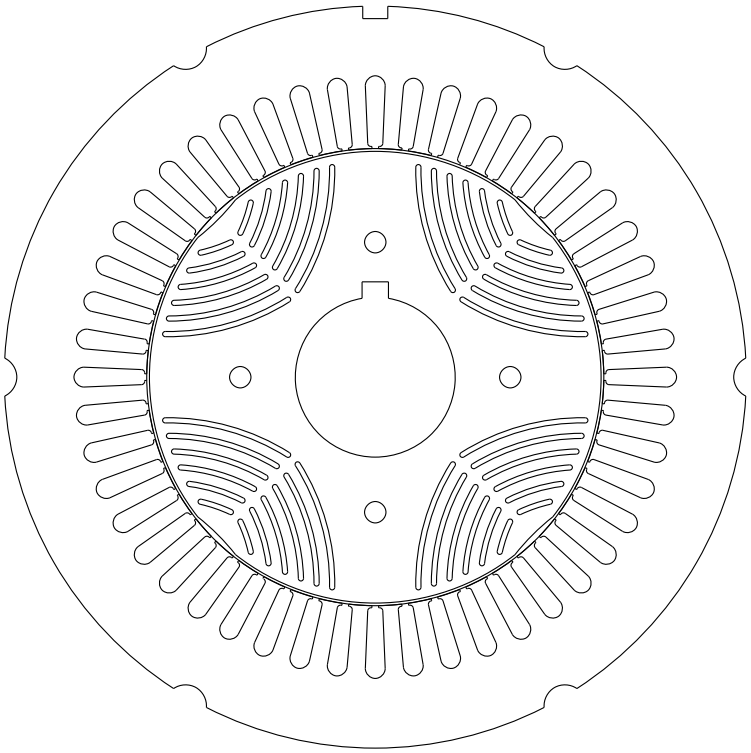


Figure 4.2: Cross section of final RSM

the RSM lags the IM in terms of torque development from 8.4% down to 4.2%. This observation reinforces the notion that a well designed RSM will not necessarily result in an optimised overall RSM drive if the control system is poorly designed and does not operate at maximum torque per ampere at all operating points.

4.4 RSM and IM thermal comparison

The rated value of an electrical machine is directly proportional to the operating temperature and tolerance of the insulation [5, 6]. The study performed by Boglietti et al. in [5] uses thermal simulations in MOTOR-CAD® to reveal the fact that a RSM does run considerably cooler than an IM as previously hypothesised in chapter 2. Thus, if desired, the user could increase the amount of current flowing in the stator windings of the RSM until the steady state temperature of the RSM reached that of the IM. It was found in [5] that the stator windings of the RSM could carry as much as 140% of the current that the IM could when at the same operating temperature. Thus, the rated value of the RSM would be higher than the original IM as a result of more current being allowed to flow in the stator windings. An electromagnetic FEM investigation is performed with 140% of the rated current

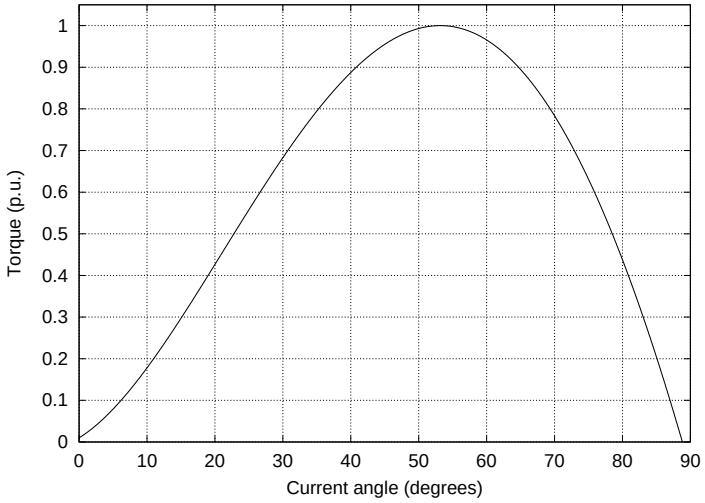


Figure 4.3: Typical RSM torque versus current angle curve

flowing in the stator windings of the RSM. The current angle is left at 60^o and the resultant torque waveform is shown in Figure 4.4. As can be seen, the average torque is just above 500 Nm which is 42% higher than the IM at rated current. Thus, the RSM has a higher rated torque density than the IM as it is capable of developing more torque than the IM while maintaining approximately the same weight and remaining in the same motor frame size. This is especially important in a traction vehicle application where high torque density of the traction motor is a primary requirement. If the analytical square relation between the stator current and the torque were obeyed (with constant inductances), as defined in equation 2.15, the torque would increase by 96% to 637 Nm. The disagreement with this can be attributed to the rotor and stator iron being driven into saturation at this overload condition. Thus, the simplified analytical relation in equation 2.15 (which assumes constant inductances) is not obeyed as a result of the torque index decreasing when more current is supplied. This effect can be clearly seen in Figure 3.25 where the torque index decreases as the current level increases.

4.5 RSM and IM comparison considering saturation

Continuing from the previous section, another observation can be made with regards to the operating point of the steel in the stator and rotor of the RSM. Consider the torque index of the designed RSM presented in Figure 3.25. When operating at rated current of 93 A rms the RSM steel is operating slightly in saturation. This

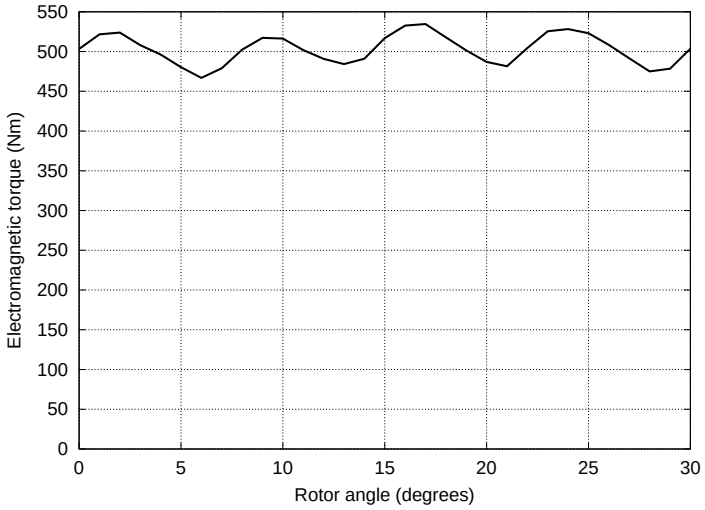


Figure 4.4: Torque of final designed RSM with 140% rated current

can be seen by the reduced torque index when the current is at 93 A rms. At this current, the torque index is 15.8 mH which is 17.6% less than the maximum torque index of 19.2 mH. If one were to match the RSM rotor and stator in the design and as a result operate closer to the maximum torque index when at rated current, the average torque will increase as a result of the increased torque index. A best case scenario would be when the torque index is at its maximum when running the RSM at rated current. If this were to occur for this RSM and equation 2.14 was used for simplification purposes, the torque generated by the final RSM design (Case III) would be 394.4 Nm if the typical current angle of $\theta_i = 60^o$ is used. This is 11% more torque than the IM. Furthermore, if a current angle that would result in MTC was used ($\theta_i = 53^o$) then the RSM would be able to generate around 411 Nm of torque (15% more than the IM). The RSM design seems promising in that it can deliver equivalent or better performance than the IM if a different rotor or stator steel were used or if an integrated rotor stator design were to be performed. An integrated rotor stator design is suggested in chapter 5 as an area of future research.

4.6 Summary

The average torque that the final RSM design develops (after electromagnetic and mechanical design) is less than the original IM by 8.4%. This gap could be halved to 4.2% if a new current angle is chosen that would allow for true MTC. Additionally, if the IM is run off a VSD it needs to be derated and thus the RSM could achieve

higher torque. The RSM is capable of developing more torque than the IM if one were to look at the situation from a thermal point of view. The RSM runs much cooler than the IM and thus more current can be placed in the stator windings until it reaches the same steady state thermal operating point as the IM. An example study revealed that with 140% rated current, the RSM develops 42% more torque than the IM when at rated current. Furthermore, when at 100% rated current, if a new type of steel were used or an integrated rotor stator design was performed for the RSM, the torque could be higher than the IM by as much as 15%. All of these results are promising as the RSM rotor will give the traction motor on the shuttle vehicle equivalent or more torque ability than the IM does while still remaining in the same motor frame size.

Chapter 5

RSM Research Suggestions and Future Work

Traditionally, suggestions for future work and improvements are included in the concluding chapter of the dissertation. However, the amount of possible future research on this topic validates the requirement for a complete chapter dedicated purely to these topics. The topics for future research are not only suggested but also briefly expanded upon to assist future researchers.

5.1 RSM design improvements

The RSM design presented in this dissertation is a first pass design that investigates the effects that various parameters have on torque development. There is a considerable amount of work that can be done on the design of the RSM to improve the design process.

5.1.1 Direct use of optimisation algorithms in FEM design

In the design procedure presented in chapter 3, a first pass design has been presented where a linear progression through all the relevant geometric parameters has been made. A new design procedure which accounts for the mutual effect of different parameters to achieve the best performance possible could be performed. This can be done in many ways, one of which is presented in the following.

In the work by Kamper et al. in [51], an optimisation algorithm is used to find a

multidimensional input vector $[X]$ which contains the machine input variables to be optimised (stator and rotor geometric parameters) that will allow for optimisation of an output function value $[Y]$ (torque, efficiency, power factor). With each iteration, the design algorithm determines the new vector direction of the search in the multidimensional space $[X]$. Line minimisation of the relevant geometric parameters is performed to maximise or minimise the function value chosen. In order to bracket the minimum or maximum of the function value $[Y]$, the input vector $[X]$ is changed in relatively large steps in a certain direction. The last three values of $[X]$ are used to curve fit a second order polynomial. From this, the maximum or minimum is found by determining where the derivative is zero.

5.1.2 Integrated rotor-stator design

A major assumption made in chapter 1 was that the same stator that was used in the original IM will be kept for the RSM. In order to allow for a more fair comparison between the RSM and the IM, the stator of the original IM should be redesigned so that a stator that is optimised to work with a RSM results. Thus, the assumption made in chapter 1 could be relaxed and an integrated rotor-stator design should be implemented since an optimal RSM rotor may not have an optimised and matched stator [7]. The best performance of the RSM will be extracted only if an integrated rotor and stator design is performed. The use of an optimisation algorithm as introduced in section 5.1.1 could be used. The multidimensional input vector $[X]$ could include not only rotor geometric parameters but also stator geometric parameters.

5.1.3 Air-gap length

Although a conservative length of air-gap is chosen in the final RSM design, in order to increase the D-axis inductance of the RSM, the length of the air-gap should be reduced relative to the original IM [6, 9]. This effect is clearly illustrated in Figure 3.12. The shorter air-gap should not be an issue as the traction vehicle motor has a relatively short stack length and thus dynamic or static eccentricity is not envisaged to be a considerable problem. The reduction of the air-gap does however increase the rotor iron losses on the rotor surface and mechanical windage losses as a result of the rotor being closer to the stator.

As a result of the suggested smaller air-gap, a suggestion made by Haataja in [6] is

to include semi-magnetic slot wedges in the stator slots. This would reduce lower order air-gap flux density harmonics which would reduce rotor iron losses and also smoothes the air-gap to reduce windage losses.

5.1.4 Choice of rotor barrier shape

In the RSM design presented, simple arcs were assumed for the shape of the rotor barriers. This seemed to be reasonable as the flux lines plotted in Figure 3.22(a) seem to line up reasonably well with the rotor barrier shape. However, in order to maximise the D-axis inductance the flux barriers should be shaped in the same way as the D-axis flux would naturally flow. Complementary to this is that the flux barriers should be at right angles to the Q-axis flux so as to minimise Q-axis inductance. The general shape of the rotor barriers can be determined by introducing a pure steel rotor without flux barriers and investigating by FEM the trajectory of the D-axis field lines with pure D-axis excitation [9]. An example of this is shown in Figure 5.1. From this, the barriers of the RSM rotor are placed to follow the D-axis field lines as best as possible. From Figure 5.1, it can be seen that the innermost barriers will have an almost *gutter like* shape but moving outwards towards the edge of the rotor the barriers would approach more of an arc shape. In [9], the flux barrier shape was based on a parabola as this is very easy to implement and a reasonable rotor barrier shape is attained. Thus, the shapes of the rotor barriers can be based on a parabolic shape that changes depending on where a rotor barrier layer is located on the rotor surface.

5.1.5 Rotor mechanical supports

The widths of the radial ribs can be graded outwards to be representative of the different mechanical stresses in the rotor [9, 19]. Also, tangential web widths can be decreased while moving from the D-axis towards the Q-axis [20]. An example of this grading of the mechanical supports is shown in Figure 5.2.

By not placing the radial ribs directly on the Q-axis the performance of the RSM may improve as a result of Q-axis flux not having a direct path to flow though. Instead, two radial ribs can be placed off the Q-axis as shown in Figure 5.3. A disadvantage of this configuration is a more intricate rotor design (where each barrier is divided into three pieces). This could drive up manufacturing costs and even weaken the mechanical strength of the rotor. However, with the mechanical FEM software

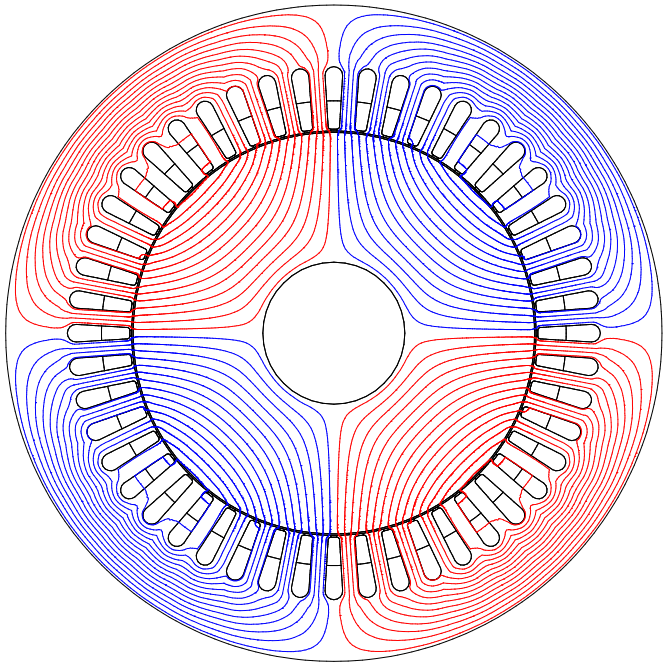


Figure 5.1: Pure steel rotor to investigate shape of D-axis flux lines

available (ANSYS®), the mechanical strength of the new rotor can be investigated quickly. The rotor may even turn out to be stronger as a result of the number of ribs doubling and also the position of the ribs (further away from the center) being required to hold in less rotor mass. As mentioned previously and as shown in Figure 5.3, the radial rib widths can also be graded outwards. At the outermost barriers, the radial ribs can even be excluded as a result of the smaller stresses when compared to the innermost barriers that need to hold in a much larger rotor mass.

5.1.6 Inclusion of rotor cage in RSM rotor

The inclusion of a rotor cage in the TL RSM rotor barriers as shown in Figure 5.4 would allow for damping of transient high torques and also allow for DOL starting [6]. It should also improve overall mechanical strength of the rotor especially at high speeds by binding the rotor structure together. The disadvantage of including a rotor cage on the RSM rotor is the loss of the major primary advantages the RSM has over the IM. That is, a cold rotor allowing the RSM to run cooler and thus be more efficient as well as allow for a higher rating. Additionally, the RSM does not need to be derated when run with a VSD like the IM.

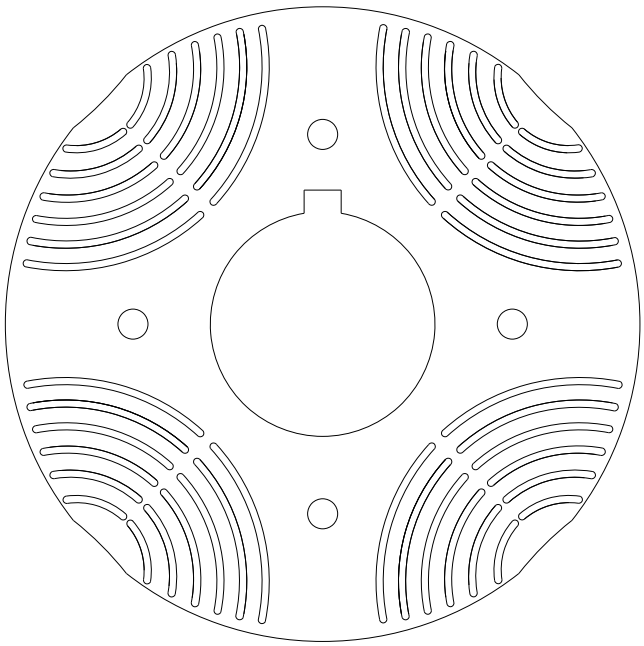


Figure 5.2: RSM rotor with graded mechanical supports

5.1.7 Torque ripple reduction

Sources of torque ripple in an electromechanical drive system can have electrical and mechanical origins. Electrically, stator slot and rotor barrier harmonics along with current time harmonics related to the control system cause torque ripple. Mechanically, ripple loads and mechanical vibrations add to overall torque ripple. In the sub-sections that follow some suggestions for torque ripple reduction are put forward.

Rotor skewing

By incorporating rotor skewing into the design of the RSM torque ripple can be reduced [17]. A concern introduced by many authors is the reduction in rated torque capability of the RSM if rotor skewing is introduced. As revealed in [17], this is unjustified if one were to consider a typical torque versus current angle curve for a RSM as shown in Figure 4.3. A zoomed view of this curve around maximum torque (where one would want to be be operating) is shown in Figure 5.5. As can be seen, the torque as a function of current angle is quite flat. Thus, for the different torque values at slightly different rotor positions when accounting for skew in the typical way, the sum of the torque generated by a set of k sub-machines displaced

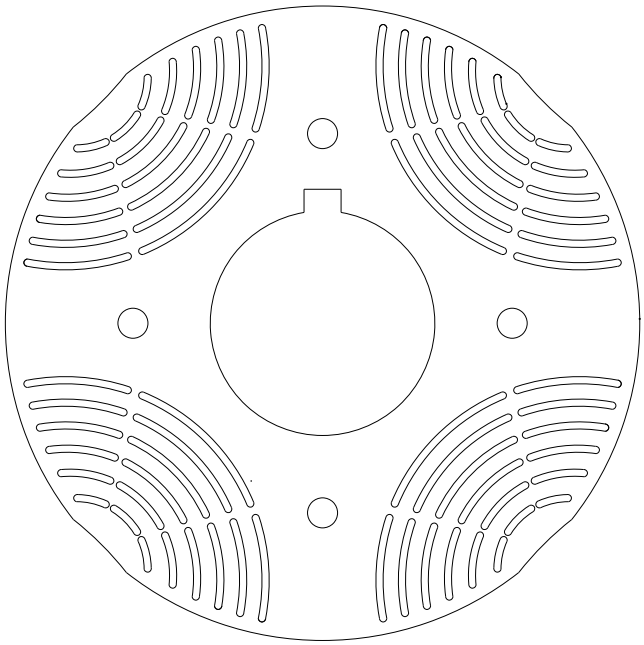


Figure 5.3: TL RSM rotor with radial ribs in new positions (off the Q-axis)

by a fraction of the skew angle divided by k, the average torque does not drop considerably but the torque ripple does.

Stator winding chording

With regards to the stator, the harmonic MMF waves in the air-gap move asynchronously with the rotor which results in torque ripple. To reduce this effect, the lower order harmonics (5th, 7th, 9th) should be reduced via reducing the relevant winding factors through chording of the stator winding as is typically done during the design of a 3-Φ AC winding [17]. It should also be noted that in some cases this stator chording has little effect on torque ripple if a small enough rotor barrier pitch is chosen. This would result in the attenuation of the ability of the asynchronous MMF waves to induce torque ripple by reaction with the rotor in the typical way [17].

Asymmetric RSM rotor design

An interesting approach taken by Sanada et al. in [52] is to design the RSM rotor asymmetrically so as to reduce torque ripple. In this approach, each rotor barrier is numbered according to it's associated pole number. Each rotor barrier edge in the first layer of rotor barriers is then shifted by a defined angle:

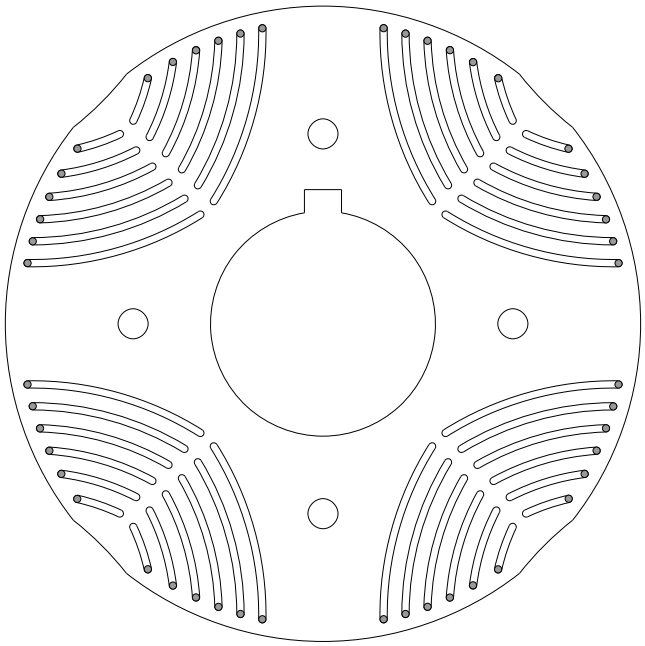


Figure 5.4: TL RSM rotor with rotor cage included in rotor barriers

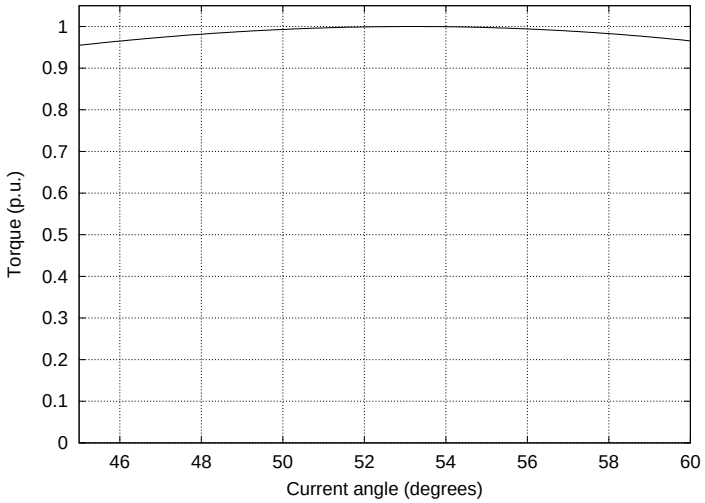


Figure 5.5: Zoomed view of typical RSM torque versus current angle

$$\psi_n = \frac{n\kappa}{2P} \tag{5.1}$$

where

ψ_n = Asymmetrical angle shift of n_{th} pole barrier

n = Relevant pole number in asymmetrical rotor design

The next layer of rotor barriers are moved by an angle relative to the inner rotor

barrier angle shift ψ_n. The asymmetrical nature of the rotor construction reduces torque substantially but results in a loss of the dynamic rotor balance. This is easily rectified by simply rotating adjacent laminations by 90^o or 180^o.

Online torque ripple reduction

In [53], online methods to reduce torque ripple have been performed where a desired torque reduction is chosen and the various gains in the control system designed around this. A torque signal is obtained from the speed feedback signal. This signal is fed back to obtain a current signal which is subtracted from the Q-axis current reference. A correctly designed compensation system allows for robustness against changes in electrical and mechanical parameters.

5.1.8 Permanent magnet assisted RSM

The problem with the conventional TL RSM rotor is that at higher speeds the power factor reduces significantly. The Permanent Magnet assisted Reluctance Synchronous Machine (PMa-RSM) should improve power factor at higher speeds and increase average torque ability as suggested by a number of authors [14, 28, 30]. The PM material (which could be cheap ferrite magnets or more expensive rare earth magnets) can be placed as shown in Figure 5.6. By introducing a small amount of these PMs into the rotor barriers of the traditional TL RSM one can improve overall performance at all speeds.

In [14], the choice of the amount of PM material to use in the rotor barriers is based on the design procedure presented in sub-section 5.1.1 where the permanent magnet dimensions in the rotor barriers were input variables in the input vector $[X]$ and the output function value $[Y]$ was the magnet volume with torque and voltage constraints placed on the design optimisation. The PM material used was a type of epoxy bonded Neodymium Iron Boron (NdFeB) magnet material which is not brittle, is easily shaped to fit into the rotor barriers and is protected against corrosion.

5.1.9 Composite powder metal RSM rotor

The conventional use of laminations for the TL rotor has the disadvantage of requiring mechanical support in the form of radial ribs and tangential webs. In [54],

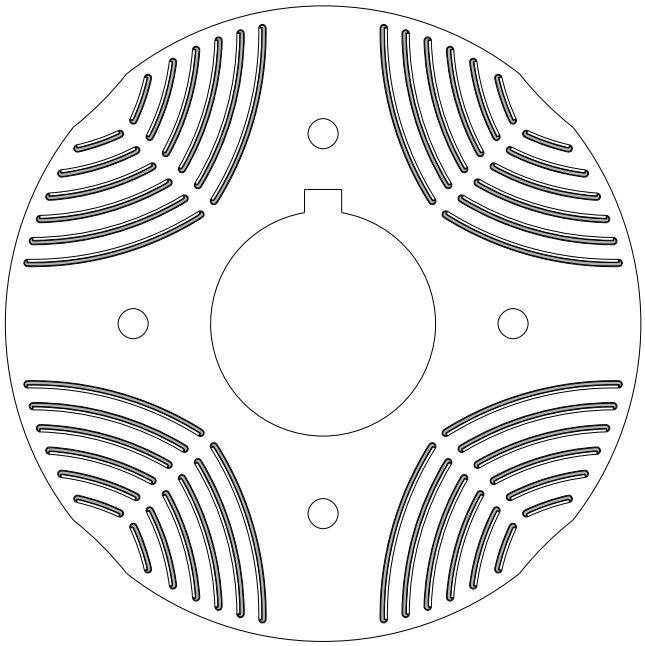


Figure 5.6: TL RSM rotor with embedded permanent magnets

the idea of using a composite powder metal for the RSM rotor is suggested. The advantages of using a composite powder metal rotor are that it will have the advantage of a high saliency ratio (similar to the ALA rotor) but with the mechanical integrity of the TL rotor to allow for high operating speeds. The composite powder metal rotor consists of two metals of approximately the same density and sintering temperature. One of the metals is ferromagnetic and the other is non-ferromagnetic. The two metals are put together in the ideally layered configuration (similar to the ALA rotor). The composite powder metal RSM could provide an alternative for obtaining better performance without the use of PMs.

5.1.10 3-D FEM analysis

The inclusion of 3-D FEM can help to take into account various 3-D effects that 2-D FEM cannot account for. These effects include end-turn leakage flux and accurately determining eddy currents (with rotor laminations being taken into account correctly). Rotor misalignment which results in static and dynamic eccentricity can also be taken into account accurately. However, the disadvantages of complex model development and high computation costs (as a result of a very high number of mesh elements) pushes designers towards using 2-D FEM for prototype development. The use of 3-D FEM only justifies its use when further in depth investigations are required by the designer to refine the prototype design.

5.2 Summary

Future work includes many aspects pertaining to the design of the Reluctance Synchronous Machine (RSM) including a better design procedure using optimisation algorithms, integrated rotor-stator design, variation of the air-gap length and the changing of flux barrier shapes to match the natural shape of D-axis flux lines. Additional design improvements could also include secondary aspects like torque ripple reduction via rotor skewing, stator chording and asymmetric rotor design. Even after these design improvements, online torque ripple reduction can be integrated into the overall control system. The inclusion of a rotor cage in the RSM rotor can also help to improve dynamic response to transient shock load requirements but would result in the loss of the cold rotor advantage the RSM has over the Induction Machine (IM). A Permanent Magnet assisted Reluctance Synchronous Machine (PMa-RSM) would result in higher average torque and power factor than the typical RSM but requires the use of expensive Permanent Magnets (PMs). A possible alternative to this is the use of composite powder metals to develop a RSM rotor. Finally, 3-D Finite Element Method (FEM) analysis can be used by the designer to refine the RSM design if required but drawbacks include complex model development and high computation time.

Chapter 6

Conclusion

Underground shuttle vehicles are essential in the underground coal mining process. The Induction Machine (IM) traction motors that drive these shuttle vehicles run very hot and it is suggested that they be replaced by a new type of motor, the Reluctance Synchronous Machine (RSM). A Transversely Laminated (TL) RSM rotor topology is suggested as a drop-in replacement for the IM rotor with the IM stator remaining intact.

RSM control requires accurate control of the current space vector angle from the D-axis. The four well known control schemes are Maximum Torque Control (MTC), Maximum Rate of Change of Torque Control (MRCTC), Maximum Power Factor Control (MPFC), Maximum Efficiency Control (MEC) and Constant Current in Inductive Axis Control (CCIAC). The current angle choice is different in each of these topologies as a result of the different control goals. In the electromagnetic design of the RSM, MTC is chosen since torque is the most important performance criteria in a traction vehicle application. The design presented can be used in the design of a RSM for any traction vehicle application since the design procedure chooses maximum average torque and minimum torque ripple as the output design criteria. The electromagnetic design of the RSM is performed using a commercially available electromagnetic Finite Element Method (FEM) software package - FLUX®. The design investigates the effects that five geometric parameters have on torque production. The geometric parameters are varied in a linear progression and a final electromagnetic design is attained by choosing where maximum average torque and minimal torque ripple occurs for each geometric parameter. Two final geometric parameters that determine mechanical strength are chosen via mechanical FEM case studies in ANSYS® after the electromagnetic design. Widths for the mechanical supports were chosen conservatively to allow for good mechanical strength.

The final RSM design develops 8.4% less torque than the original IM when operating at rated current. However, the IM is often derated due to it being run with a VSD and thus the RSM should be able to generate more torque than the IM. Also, if the RSM were operated at exactly maximum torque per ampere then it would develop only 4.2% less torque than the IM. Furthermore, the RSM is capable of carrying more current in the stator windings (without overheating) and thus develops more torque than the IM for the same motor frame size. It has been shown that the RSM can develop more than 40% more torque than the IM while still operating at the same temperature. It has also been shown that if the RSM were to operate with less saturation and thus a higher torque index, it could develop up to 15% more torque than the IM even if only rated current were to be supplied to the RSM. The designed RSMs' ability to develop torque comparable to the original IM at rated current and in some cases more torque than the original IM makes it a viable alternative in traction vehicle applications.

References

[1] T. Novak, J. Meigs, and R. Sanford, "Development of an expert system for diagnosing component level failures in a shuttle car," *IEEE Transactions on Industry Applications*, vol. 25, pp. 691–698, July/Aug. 1989.

[2] P. Kovalchik, "Thermal characteristics of reeled trailing cables for shuttle cars," *12th WVU International Mining Electrotechnology Conference*, pp. 91–94, July 1994.

[3] D. Staton, T. Miller, and S. Wood, "Optimisation of the synchronous reluctance motor geometry," *Fifth International Conference on Electrical Machines and Drives*, pp. 156–160, Sep. 1991.

[4] A. Vagati, "The synchronous reluctance solution: A new alternative in a.c. drives," *20th International Conference on Industrial Electronics, Control and Instrumentation*, vol. 1, pp. 1–13, Sep. 1994.

[5] A. Boglietti, A. Cavagnino, M. Pastorelli, D. Staton, and A. Vagati, "Thermal analysis of induction and synchronous reluctance motors," *IEEE International Conference on Electric Machines and Drives*, vol. 1, pp. 1592 – 1597, May 2005.

[6] J. Haataja, "A comparative performance study of four-pole induction motors and synchronous reluctance motors in variable speed drives," Ph.D. dissertation, Lappeenranta University of Technology, Lappeenranta, Finland, June 2003.

[7] A. Fratta, A. Vagati, "A reluctance motor drive for high dynamic performance applications," *IEEE transactions on industry applications*, vol. 28, pp. 873–879, 1992.

[8] A. Vagati, A. Fratta, G. Franceschini, and P. Rosso, "Ac motors for high-performance drives: a design-based comparison," *IEEE Transactions on Industry Applications*, vol. 32, pp. 1211 – 1219, Sept./Oct. 1996.

[9] J. Germishuizen, F. Van der Merwe, K. Van der Westhuizen, and M. Kamper, "Performance comparison of reluctance synchronous and induction traction drives for electrical multiple units," *Conference Record of the 2000 IEEE Industry Applications Conference*, vol. 1, pp. 316–323, 2000.

[10] D. Staton, W. Soong, and T. Miller, "Unified theory of torque production in switched reluctance and synchronous reluctance motors," *IEEE Transactions on Industry Applications*, vol. 31, pp. 329–337, Mar./Apr. 1995.

[11] D. Staton, W. Soong, R. Deodhar, and T. Miller, "Unified theory of torque production in ac, dc and reluctance motors," *Conference Record of the 1994 IEEE Industry Applications Society Annual Meeting*, vol. 1, pp. 149–156, Oct. 1994.

[12] T. Matsuo and T. Lipo, "Rotor design optimization of synchronous reluctance machine," *IEEE Transaction on Energy Conversion*, vol. 9, pp. 359–365, June 1994.

[13] D. Staton, T. Miller, and S. Wood, "Maximising the saliency ratio of the synchronous reluctance motor," *IEE Proceedings: Electric Power Applications*, vol. 140, pp. 249 – 259, July 1993.

[14] S. Sibande, M. Kamper, R. Wang, and E. Rakgati, "Optimal design of a pm-assisted rotor of a 110 kw reluctance synchronous machine," in *Proc. 7th AFRICON Conference in Africa AFRICON*, vol. 2, 2004, pp. 793–797 Vol.2.

[15] I. Boldea and S. Nasar, *The Induction Machine Handbook*. CRC Press LLC, 2002.

[16] I. Boldea, Z. Fu, and S. Nasar, "Performance evaluation of axially-laminated anisotropic (ala) rotor reluctance synchronous motors," *IEEE Transacions on Industry Applications*, vol. 30, pp. 977–985, Jul./Aug. 1994.

[17] X. Bomela and M. Kamper, "Effect of machine design on performance of reluctance synchronous machine," *Conference Record of the 2000 IEEE Industry Applications Conference*, vol. 1, pp. 515–522, 2000.

[18] R. Betz, R. Lagerquist, M. Jovanovic, T. Miller, and R. Middleton, "Control of synchronous reluctance machines," *IEEE transactions on industry applications*, vol. 29, pp. 1110–1122, Nov./Dec. 1993.

[19] F. Leonardi, F. Leonardi., P. McCleer, and A. Elantably, "Rotors for synchronous reluctance traction motors: a comparative study," in *Thirty-Fourth IAS Annual Meeting Industry Applications Conference Conference Record of the 1999 IEEE*, P. McCleer, Ed., vol. 2, 1999, pp. 835–839.

[20] A. Vagati, M. Pastorelli, G. Franceschini, and C. Petrache, "Design of low-torque-ripple synchronous reluctance motors," in *Conference Record of the 1997 IEEE Industry Applications Conference Thirty-Second IAS Annual Meeting, IAS '97*, vol. 1, 1997, pp. 286–293 vol.1.

[21] A. Vagati, A. Canova, M. Chiampi, M.Pastorelli, and M. Repetto, "Design refinement of synchronous reluctance motors through finite element analysis," *IEEE Transactions on Industry Applications*, vol. 36, pp. 1094–1102, Jul./Aug. 2000.

[22] R. Trubenbach, R. Trubenbach, A. Mackay, and M. Kamper, "Performance of a reluctance synchronous machine under vector control," in *Proc. th Annual*

IEEE Power Electronics Specialists Conference PESC '93 Record, A. Mackay, Ed., 1993, pp. 803–808.

[23] M. Rohde, "Modification of an induction motor for synchronous reluctance machine application," Master's thesis, School of Electrical and Information Engineering, University of the Witwatersrand, 1997.

[24] T. Lubin, H. Razik, and A. Rezzoug, "On-line efficiency optimization of a synchronous reluctance motor," *ScienceDirect, Electric Power Systems Research*, 2006.

[25] L. Xu and J. Yao, "A compensated vector control scheme of a synchronous reluctance motor including saturation and iron losses," *IEEE Transactions on Industry Applications*, vol. 28, pp. 1330 – 1338, 1992.

[26] L. Xu, X. Xu, T. Lipo, and D. Novotny, "Vector control of a synchronous reluctance motor including saturation iron loss," *IEEE transactions on industry applications*, vol. 27, pp. 977–985, Sep./Oct. 1991.

[27] R. Betz, M. Jovanovic, R. Lagerquist, and T. Miller, "Aspects of the control of synchronous reluctance machines including saturation and iron losses," *Conference Record of the 1992 IEEE Industry Applications Society Annual Meeting*, vol. 1, pp. 456 – 463, Oct. 1992.

[28] H. de Kock and M. Kamper, "Dynamic control of the permanent magnet-assisted reluctance synchronous machine," *IET Electric Power Applications*, vol. 1, pp. 153 – 160, Mar. 2007.

[29] S. Ichikawa, S. Ichikawa, M. Tomita, S. Doki, and S. Okuma, "Sensorless control of synchronous reluctance motors based on extended emf models considering magnetic saturation with online parameter identification," *IEEE Transactions on Industry Applications*, vol. 42, no. 5, pp. 1264–1274, Sept./Oct. 2006.

[30] P. Niazi, "Permanent magnet assisited synchronous reluctance motor design and performance improvement," Ph.D. dissertation, School of Electrical Engineering, Texas A&M University, 2005.

[31] I. Boldea, C. Pitic, C. Lascu, G. Andreescu, L. Tutelea, F. Blaabjerg, and P. Sandholdt, "Dtfc-svm motion-sensorless control of a pm-assisted reluctance synchronous machine as starter-alternator for hybrid electric vehicles," *IEEE Transactions on Power Electronics*, vol. 21, pp. 711– 719, May 2006.

[32] M.-H. Kim, N.-H. Kim, D.-H. Kim, S. Okuma, and J. Hung, "A position sensorless motion control system of reluctance synchronous motor with direct torque control," *Proceedings of the 2002 IEEE International Symposium on Industrial Electronics*, vol. 4, pp. 1148– 1153, 2002.

[33] M. Javanovic, R. Betz, and D. Platt, "Sensorless vector controller for a synchronous reluctance motor," *IEEE transactions on industry applications*, vol. 34, pp. 346–354, Mar./Apr. 1998.

[34] R. Betz, "Theoretical aspects of control of synchronous reluctance machines," *IEE Proceedings Electric Power Applications*, vol. 139, pp. 355 – 364, July 1992.

[35] I. Boldea, N. Muntean, and S. Nasar, "Robust low-cost implementation of vector control for reluctance synchronous machines," *IEE Proceedings - Electric Power Applications*, vol. 141, pp. 1–6, Jan. 1994.

[36] H. Hofmann, S. Sanders, and A. El-Antably, "Stator-flux-oriented vector control of synchronous reluctance machines with maximised efficiency," *IEEE transactions on industry applications*, vol. 51, pp. 1066–1072, Oct. 2004.

[37] P. Hudak, V. Hrabovcova, P. Rafajdas, and J. Mihok, "Core loss analysis of the reluctance synchronous motor with barrier rotors," *Journal of Electrical Engineering*, vol. 55, pp. 273–276, 2004.

[38] D. Miljavec, P. Jereb, and M. Popovic, "Pulsating losses in synchronous reluctance motor," *Electrical Machines and Drives*, vol. Conference Publication No. 412, pp. 261–265, 1995.

[39] F. Fernandez-Bernal, F. Fernandez-Bernal, A. Garcia-Cerrada, and R. Faure, "Efficient control of reluctance synchronous machines," in *Proc. 24th Annual Conference of the IEEE Industrial Electronics Society IECON '98*, A. Garcia-Cerrada, Ed., vol. 2, 1998, pp. 923–928 vol.2.

[40] T. Matsuo, T. Matsuo, A. El-Antably, and T. Lipo, "A new control strategy for optimum-efficiency operation of a synchronous reluctance motor," *IEEE transactions on industry applications*, vol. 33, pp. 1146–1153, Sep./Oct. 1997.

[41] N. Bianchi, *Electrical Machine Analysis Using Finite Elements*. CRC Press Ltd, 2005.

[42] R. Ferrarri and P. Silvester, *Finite elements for Electrical Engineers*, 3rd ed. Cambridge University Press, 1996.

[43] S. Salon, *Finite Element Analysis of Electrical Machines*. Kluwer Academic Publishers, 1995.

[44] J. Bastos and N. Sadowski, *Electromagnetic Modeling by Finite Element Methods*. Marcel Dekker Inc., 2005.

[45] J. Coulomb and G. Meunie, "Finite element implementation of virtual work principle for magnetic or electric force and torque computation," *IEEE Transactions on Magnetics*, vol. MAG-20, NO. 5, pp. 1894–1896, Sept. 1984.

[46] P. Hudak, H. V., and P. Rafajdas, "Geometrical dimension influence of multi-barrier rotor on reluctance synchronous motor performances," *International Symposium on Power Electronics, Elctrical Drives, Automation and Motion*, pp. 346 – 351, May 2006.

[47] A. K. Kaw and E. E. Kalu, *Numerical Methods with Applications*, *http : //numericalmethods.eng.usf.edu/topics/textbook$_i$ndex.html*, Ed. World Wide Web, http://www.autarkaw.com, 2009.

[48] Y. Saad and M. Schultz, "Gmres: A generalised minimal residual algorithm for solving nonsymmetric linear systems," *Journal on Scientific and Statistical Computing*, vol. 7, pp. 856 – 869, July 1986.

[49] Y. Saad, "Ilut: A dual threshold incomplete lu factorization," *Numerical Linear Algebra with Applications*, vol. 1, pp. 387–402, 1994.

[50] J. Wright, W. Cronje, and A. Meyer, "Dynamic fem modelling and laboratory verification of a 3-phase squirrel cage induction machine," *Proceedings of the 8th International Symposium on Electric and Magnetic Fields*, 2009.

[51] M. Kamper, F. Van der Merwe, and S. Williamson, "Direct finite element design optimisation of the cageless reluctance synchronous machine," *IEEE transaction on energy conversion*, vol. 11, pp. 547–555, Sep. 1996.

[52] M. Sanada, K. Hiramoto, S. Morimoto, and Y. Takeda, "Torque ripple improvement for synchronous reluctance motor using asymmetric flux barier arrangement," *IEEE transactions on industry applications*, vol. 40, pp. 1076–1082, 2004.

[53] J. Zhao, J. Zhao, M. Kamper, and F. van der Merwe, "On-line control method to reduce mechanical vibration and torque ripple in reluctance synchronous machine drives," in *Proceedings 23rd International Conference on Industrial Electronics, Control and Instrumentation*, M. Kamper, Ed., vol. 1, 1997, pp. 126–131 vol.1.

[54] F. Reiter Jr and T. Stuart, "Composite powder metal synchronous reluctance machine," *IEEE International Electric Machines and Drives Conference, 2003*, vol. 1, pp. 523– 527, 2003.

Appendix A

Example Python File used in electromagnetic design

An example Python file that is used during the electromagnetic design procedure can be found in Listing A.1. The example Python file in Listing A.1 is the Python file used to vary the geometric parameter W_p, Each of the Python files used in the electromagnetic design have the same fundamental file structure as that of Listing A.1 and are only changed slightly to reflect the different parameter being changed

Listing A.1: Example Python file used during electromagnetic design

```
#! Preflu2D 10.2

################################Setup Solving Process#############################################

#Define rotor range and resolution
minRotorPos = 0.0;
maxRotorPos = 30.0;

#Define solving parameters
rotorStep = 1.0;
precisionValue = 0.01;
IterationValue = 20;

#Name the scenario relevant to parameter being changed
scenarioName = 'RSM-Design-NRB-WP';
Scenario(name=str(scenarioName))
Scenario[str(scenarioName)].addPilot(pilot=MultiValues(parameter=VariationParameter['ANGPOS_ROTOR'],
      intervals=[IntervalStepValue(minValue=minRotorPos, maxValue=maxRotorPos, stepValue=rotorStep)]))

#Define the solving options
SolvingOptions['SOLVING_OPTIONS'].newtonRaphsonParameters=
```

```
22          ParametersNewtonRaphson(precision=precisionValue,maximumIterationNumber=IterationValue,
23          relaxationFactorComputationMethod=
24          ParametersNewtonRaphsonRelaxationFactorComputationMethodAutomatic())
25
26
27  ##########################Solve the problem domain, parameterised#########################################
28
29  #Define array of values for parameter to be varied (W_{p})
30  wpArray = [15, 20, 25, 30, 35, 40, 45, 50, 55, 60, 65, 70];
31
32  #In order for a geometric parameter to be changed the mesh needs to be deleted
33  deleteMesh()
34
35  #Start of loop that runs through array of geometric parameter values for W_{p}
36  for i in wpArray:
37          #So the mesh is deleted for next parameter to be changed
38          deleteMesh()
39          #The value in the array is assigned to a dummy variable
40          wpValue = i;
41          #The parameter is changed in the geometry
42          ParameterGeom['wp'].expression=str(wpValue)
43
```

```
#Mesh the geometry again so it is ready for solving
meshLines()
meshFaces()

#Solve the project
Scenario[str(scenarioName)].solve(projectName='RSM-Design-NRB-WP.FLU')

#Post-processing
#Name the torque so that it can be assigned to a torque waveform and file name
torqueName = 'torque-NRB-WP-WP'+str(wpValue);
#Extract the torque versus rotor angle waveform
EvolutiveCurve2D(name=str(torqueName),
evolutivePath=
EvolutivePath(parameterSet=[SetParameterXVariable(paramEvol=VariationParameter['ANGPOS_ROTOR'],
limitMin=minRotorPos,limitMax=maxRotorPos)]),formula=['TorqueElecMag(ROTOR)']);
#Show the torque waveform in FLUX
Curve2d[str(torqueName)].visible=0
#Export the torque waveform to a text file with the relvant file name
CurveVariation2D[str(torqueName)].exportTXT(txtFile=str(torqueName), mode='REPLACE_FILE')

#Edit text file for interpretation by Octave
fileName = torqueName+".txt";
```

```
66  fileIN = open(str(fileName), "r")
67  lineList = fileIN.readlines()
68  lineCount =  0;
69  for line in lineList:
70          lineCount = lineCount+1;
71  Filelength = lineCount;
72  setStart = 0;
73  setEnd = 0;
74  for i in range(Filelength):
75          if lineList[i]=='  Column 1         Column 2         \n':
76                  setStart = i+1;
77          if lineList[i]=='Mean values:\n':
78                  setEnd = i-2;
79  numSteps = setEnd-setStart+1;
80  outfile = open(str(fileName), "w+")
81  for i in range(numSteps):
82          outfile.write(lineList[setStart+i]);
83  outfile.close()
84  fileIN.close()
85
86  #Delete old results so same scenario can be used with new geometric parameter value W_{p}
87  Scenario[str(scenarioName)].deleteAllResults()
```

```
88
89 saveProject('RSM-Design-NRB-WP.FLU')
90 closeProject()
```

Appendix B

Geometric details of the RSM design

B.1 Stator geometric details

The geometric details (in millimetres) of one stator slot are shown in Figure B.1. As can be seen, the air-gap is left at the nominal value of 0.8 mm. A cross section of a full stator lamination is given in Figure B.2. As can be seen, a 48-slot semi-enclosed stator is used. The required stator mechanical supports include the weld recesses (6 equally spaced around the stator outer periphery) as well as the stator key-way.

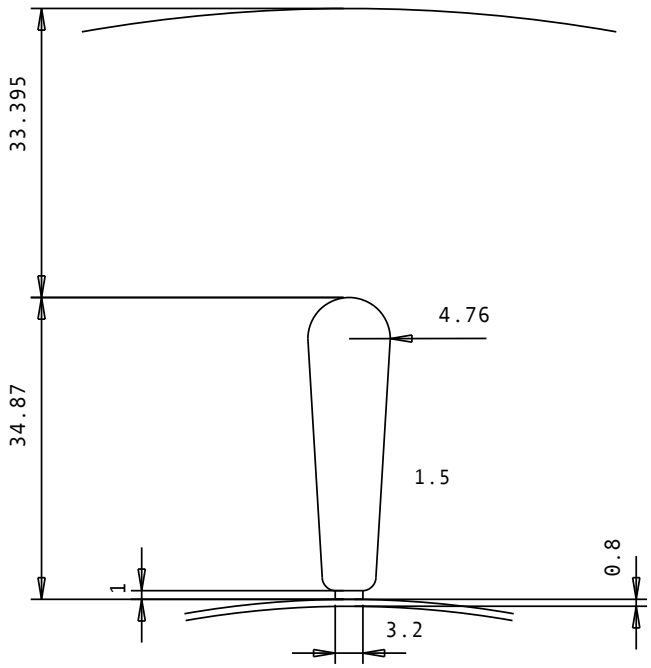


Figure B.1: Geometric dimensions of one stator slot

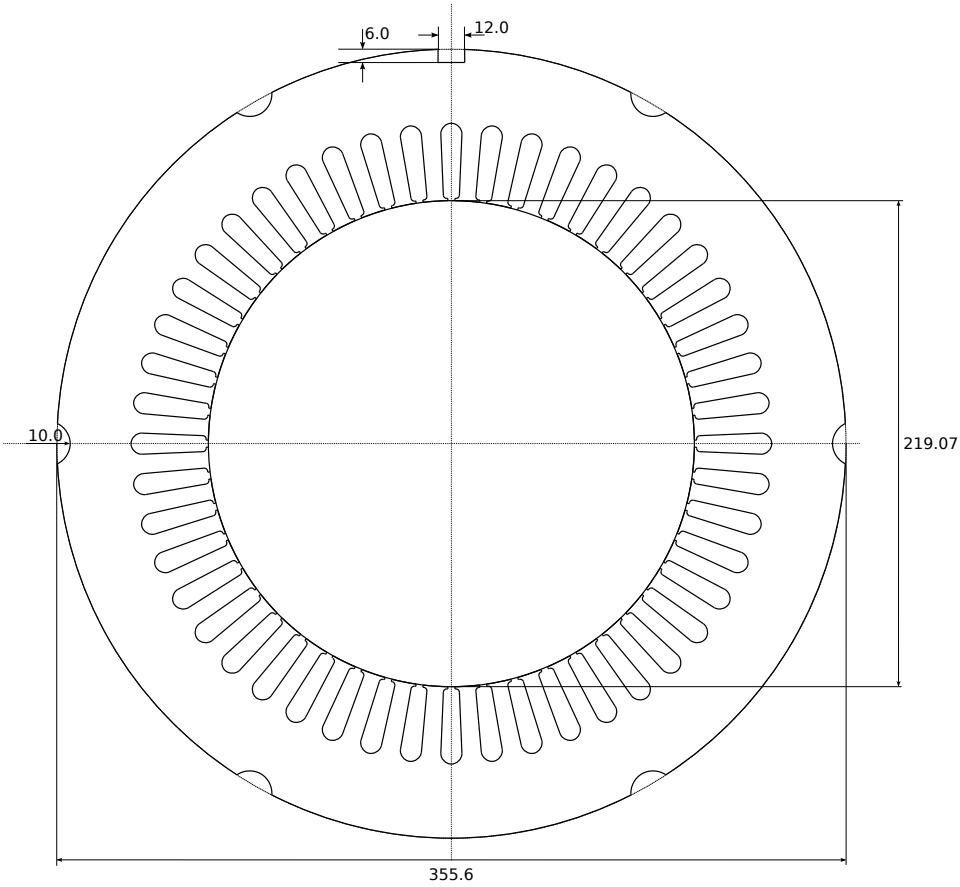


Figure B.2: Geometric dimensions of stator lamination

B.2 Rotor geometric details

The geometric details (in millimetres) of the final RSM rotor are shown in Figure B.3. The geometric values shown here correlate with the final RSM design after the electromagnetic FEM design and mechanical case studies were performed.

B.3 Final stator and rotor

The cross section of the final RSM rotor inside the original 48-slot stator is shown in Figure B.4.

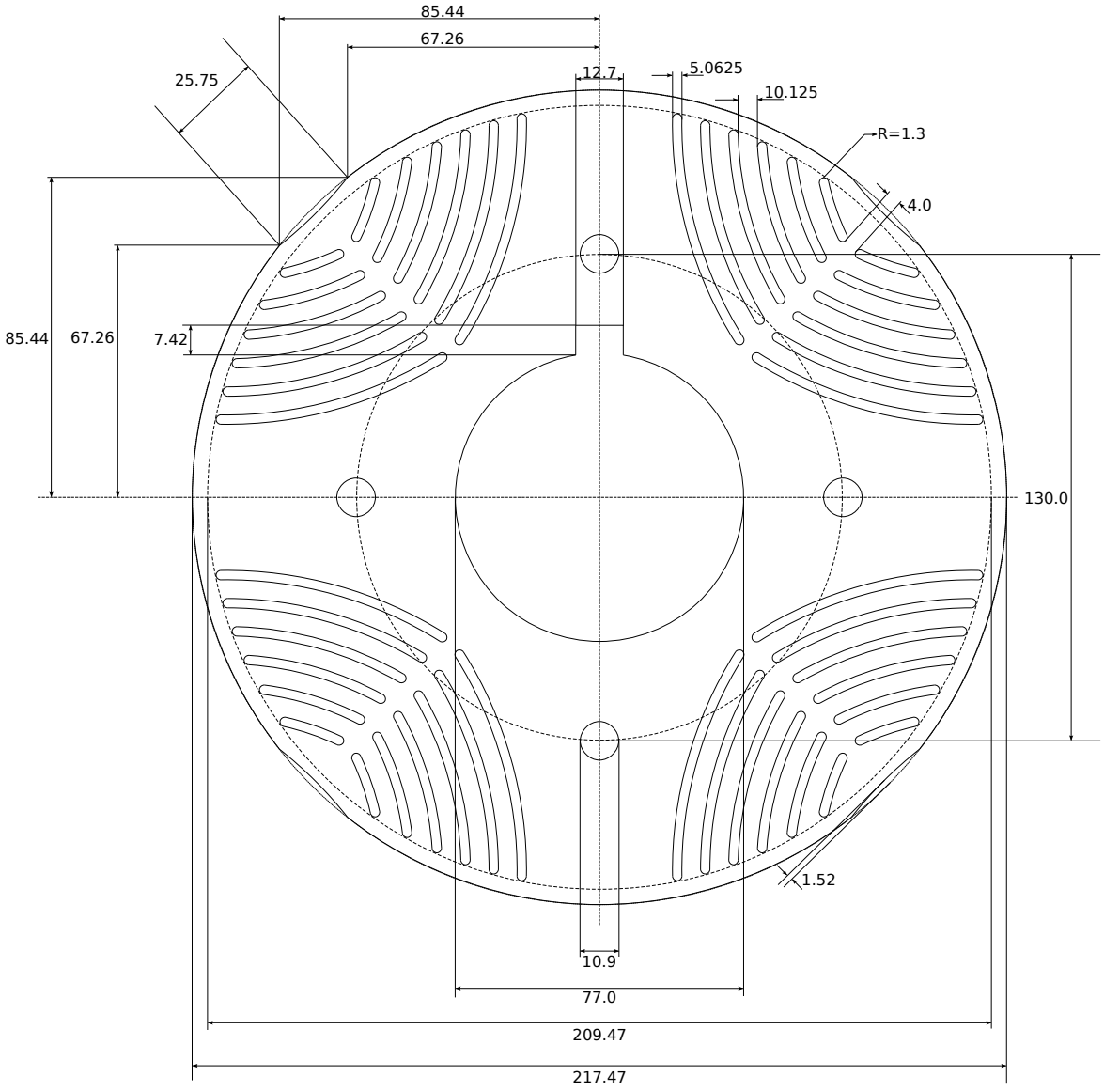


Figure B.3: Geometric details of final RSM rotor lamination

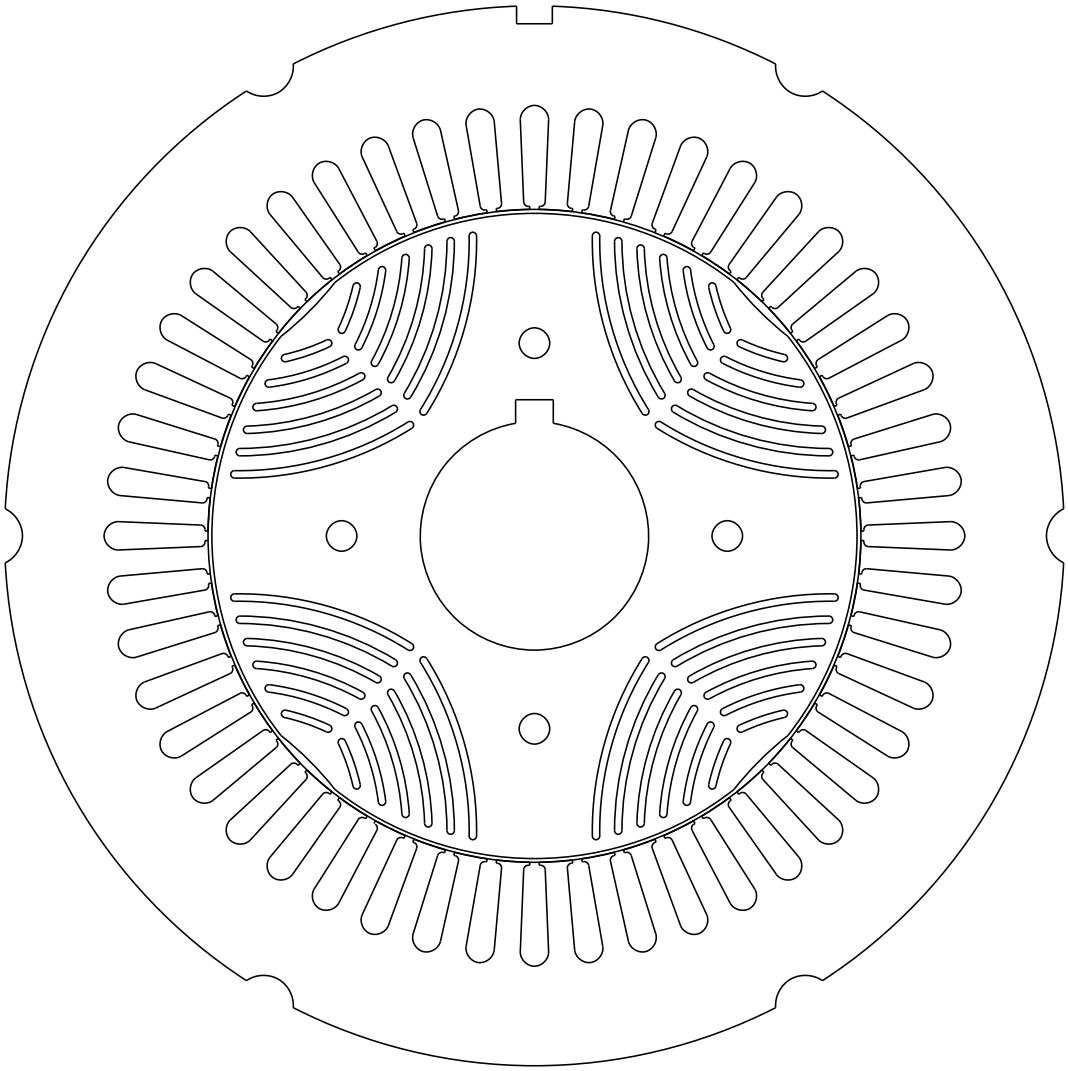


Figure B.4: Final RSM rotor inside original stator

Appendix C

Technical details of original IM

A cross section of the modelled original IM is repeated in Figure C.1 for convenience. The technical details of the original IM used for the traction motor in the underground shuttle vehicle are given in Table C.1.

Table C.1: Original IM technical specifications

Parameter	Value
Number of stator slots	48
Number rotor bars	38
Air-gap length (mm)	0.8
Circuits in parallel	2
Span	1-10
Conductors in parallel	5
Number of turns per phase	5
Frequency (Hz)	50
Poles	4
Phase voltage (V)	440
Phase current (A)	93
Nominal speed (rpm)	1478
Nominal torque (Nm)	355

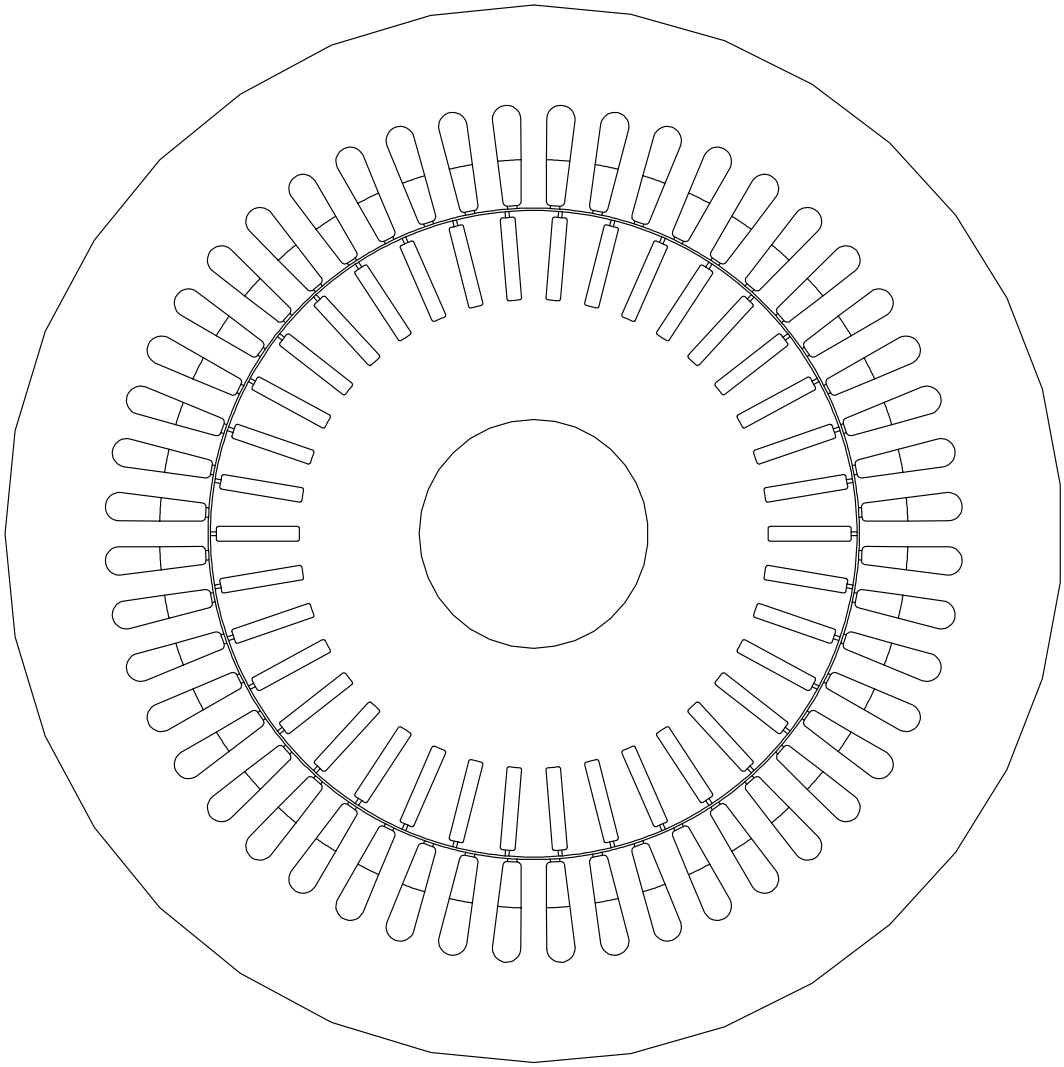


Figure C.1: Cross section of modelled original IM

Appendix D

Published Work

The papers published on the work in this dissertation are listed:

- J. Wright, W. Cronje and A.Meyer, "FEM Modeling and Preliminary Simulation Results of a 3-Phase Squirrel Cage Induction Machine," Proceedings of the 18^{th} Southern African Universities' Power Engineering Conference (SAUPEC), pp. 30-35, Jan. 2009.
- J. Wright, W. Cronje and A.Meyer, "Dynamic FEM Modelling and Laboratory Verification of a 3-Phase Squirrel Cage Induction Machine," 8^{th} International Symposium on Electric and Magnetic Fields (EMF), May 2009.
- J. Wright, W. Cronje and A.Meyer, "Dynamic Design of a Reluctance Synchronous Machine utilising Python Scripting in FLUX 10.2," FLUX User's Conference, Oct. 2009.
- J. Wright and W. Cronje, "The Electromagnetic and Mechanical Design of a Reluctance Synchronous Machine Rotor Using the Finite Element Method", Proceedings of the 19^{th} Southern African Universities Power Engineering Conference (SAUPEC), pp. 48-54, Jan. 2010.